University of Stavanger

Faculty of Science and Technology

BACHELOR`S THESIS

Study program/Specialization:	
Kjemi og miljø	Autumn semester, 2021 Open / Restricted access

Writer:	
John Arild Solvang Lindberg	X _____ John Arild Solvang Lindberg (Writer's signature)

Faculty supervisor:

Sachin M. Chavan

Thesis title:

Metal-organic frameworks for the recovery of critical metals for batteries

Credits (ECTS):

Key words:	
Lithium, recovery, adsorption, MOF, metal-organic framework, green-synthesis, UiO-66, BDC-COOH, BDC-$(COOH)_2$, zirconium-MOF	Pages: ……37…… + enclosure: ……20…… Stavanger, ……31.12.2021….. Date/year

Foreword

This thesis deals with enrichment of lithium from dilute sources by adsorption with metal-organic frameworks (MOFs) as adsorbent. Technologies and methods invented to benefit the environment and to battle climate change is of interest to me as I think it's rewarding to be a part of the solution to the problems we face as a society. I also found MOFs and their wide relevance of various applications to be an interesting case of study. I think MOFs will be a much used material in the future and for many applications, and so to learn so extensively about them felt like a great opportunity.

Abbreviations used in this thesis

MOF	Metal-organic framework
PXRD	Powder x-ray diffraction
cP	Primitive cubic system
bcc	Body-centered cubic
fcc	Face-centered cubic
TGA	Thermogravimetric
SBU	Secondary building unit
REM	Rare earth metals
PGM	Platinum-group metals
SEM	Scanning electron microscopy
EDS	Energy dispersive spectroscopy
UiO	Universitetet i Oslo
PE	Primary electron
SE	Secondary electron
BSE	Back-scattered electron
FW	Formula weight
IR	Infrared spectroscopy
ICP	Inductively coupled plasma
OES	Optical emission spectroscopy
BET	Brunauer–Emmett–Teller theory
BDC	Benzene-1,4-dicarboxylic acid

Summary

Lithium mining is a much sought after metal that is essential in many green technologies, especially battery technology. With the rising pressure on the planet's climate a shift to greener alternatives is growing and with it demand for lithium. The current mining of lithium is however inefficient and resource intensive in regards to water and land areal.

To address this challenge a new method for extracting lithium utilising adsorbents is being explored. A shortcoming of many adsorbents used in the treatment of water is low porosity (and lack of selectivity). Prospects in regards to adsorption will likely involve synthetic crystalline materials called metal-organic frameworks (MOFs). MOFs combine inorganic and organic building units, metal ions/clusters and linkers respectively.

These materials have been shown to possess much greater porosity and inner surface area. So far most research activities have focused on gas adsorption using MOFs as most are unstable in water. Water stability has been a challenge, fortunately, a large number of MOF structures have been discovered, and, opportunely from the University of Oslo in Norway a series of water-stable zirconium-based MOFs have been reported [7].

This thesis work will use the opportune Zr-cluster based MOFs with carboxylate functional groups that could be sites of ion exchange interaction. In particular two MOFs with 1,2,4-Benzenetricarboxylic acid (BDC-COOH) and 1,2,4,5-Benezenetetracarboxylic acid (BDC-$(COOH)_2$) are explored in this thesis. MOF characteristics have been determined using powder x-ray diffraction, thermogravimetric analysis, nitrogen adsorption, scanning electron microscope with energy dispersive x-ray spectrometry, and infrared spectroscopy. Furthermore, MOF samples synthesised are used to carry out batch adsorption experiments to find whether they are applicative for metal ion uptake in water solution. Two studies were set up, where five vials of different metal ion concentration, one with lithium chloride and the other with magnesium chloride, had MOF samples added to them and were left to adsorb overnight.

UiO-66-BDC-COOH and Zr-BDC-$(COOH)_2$ were both successfully synthesised and employed in metal adsorption studies. Samples JA01 and JA04 were chosen as adsorbents since they showed the strongest results after characterisation analysis. JA01 and JA04 syntheses were upscaled (JA09 and JA10 respectively) to have enough quantity for batch adsorption.

JA09 proved not to be chemically stable in water. JA10 did not show any sign of significant metal ion uptake. Likely the problem was the low pH value. Solutions after adsorption experiment turned out to be much more acidic, and showed greater conducitivity than before adsorption.

Table of contents

1. Introduction

1.1 Background to thesis work

An increase in carbon dioxide in the atmosphere since the industrial revolution has led to global warming, where the arctic is melting which is causing the sea level to rise. To combat climate change 194 states along with the European Union [1] have come together and signed the Paris Agreement, a legally binding treaty created to deal with climate change. Its goals are among others explicitly to limit the rise in temperature globally to preferably 1.5 °C, and not more than 2 °C, more than pre-industrial levels [2].

To slow down the rise in temperature the world is shifting towards renewable and more sustainable technologies and sources of energy. One such avenue is the shift from vehicles relying on petrol from oil to partial or fully electrification. This is achieved by employing battery technology, and lithium-ion batteries are the dominant choice of energy source in many electric vehicles [3]. Lithium is also used in electric devices like mobile cell phones, ceramics, heat-resistant glass, medicine, iron flux additives, and for the production of steel and aluminium [4][5][6].

Lithium is a highly sought after material because of its properties. It is a light weight, highly reactive alkali metal and is considered a soft metal. It has a single electron in its outer shell, making it monovalent. Lithium also has good heat and electrical conductivity. Additionally, lithium ions have the ability to move from positive potential to negative. This is what makes lithium such a sought after material in battery technologies as it opens up the posibility to recharge the battery. Because of lithium's highly reactive nature, it's not found as a pure elemental in nature. Lithium is instead found as components of salts and other compounds.

Lithium reserves on land are found in places such as underground deposits of clay, in mineral ore, or in pockets of underground water. Lithium reserves are also in seawater and can be found in geothermal and oil fields well brines as well [5]. Brines have become the main source of lithium [11]. According to Sterba et al. brines account for 66% of global lithium resources [5]. The current method for extraction of lithium from brines is by collecting great quantities of water from lakes, underground or the sea, and to then leave it to evaporate via solar radiation. As the brine evaporates salts precipitate and the higher lithium concentrated brine left is moved to another pool so the salts can be collected. This method is inefficient because lithium needs to be 99% pure, but co-precipitates with magnesium, and so lithium is lost during the mining process.

This extraction method is a lengthy process, requires large amounts of water and great areas of land, which in turn affects the environment. The ecosystems touched by mining and extraction are disrupted. Local communities lose water that could have been used as a source of drinking water or used for farming. There is also the issue of where to put all the loose mass of rock, gravel, and clay after digging out the pools. Public outcry may lead to restrictions that affect the lithium reserves and with it the lithium production. Furthermore, as the demand for lithium increases as in turn will the pressure on lithium extraction increase. Tables 1 and 2 give data of extraction and reserves vs resources, respectively.

Country	2015	2016	2017	2018	2019
Argentina[d,e]	20 073	30 877	31 060	34 712	34 278
Australia	439 514	522 181	1 706 619	1 965 944	1 616 764
Bolivia[d]	-	162	*60	*230	*400
Chile[f]	56 375	78 182	81 378	97 323	112 607
China[c]	*3 900	*4 800	*7 000	*7 100	*7 500
USA[c]	*900	*900	*900	*900	*900
Zimbabwe	44 000	48 000	51 000	70 000	65 000

Table 1. World mineral production from British Geological Survey, numbers given in tonne of metal content [12]. Note: Letters denote mineral source a) Lepidolite, b) spodumene, c) Li content, d) Carbonate, e) Chloride, f) Carbonate, hydroxide, and chloride. The star symbol '*' denotes estimate.

Country	Reserves	Resources
Argentina	1 900 000	19 300 000
Australia	4 700 000	6 400 000
Bolivia	-	21 000 000
Chile	9 200 000	9 600 000
China	1 500 000	5 100 000
USA	750 000	7 900 000
Zimbabwe	220 000	500 000

Table 2. A section of *Reserves versus resources of lithium*, given in tonnes, from U.S. Geological Survey, 2021 [3][6].

For this reason, a new method of mining lithium is being explored, which involves the use of adsorbents to extract lithium from brine. The adsorption desorption could make the process of extracting lithium more efficient and in turn, reduce the water load which would lessen the negative environmental impact. The various adsorbents used to treat water in the literature are the bark, lignin, chitosan, zeolite, clay, activated carbon, alumina, polymers, resins, and so forth [20][30]. Typical adsorbents like zeolites are relatively small in pore size. A prospective, state of the art, kind of porous materials called MOFs have shown great porosity, although very few are stable in water.

1.2 Metal-organic frameworks

The scope of this thesis is limited to the zirconium cluster-based MOFs bearing free carboxylic acid functionality, but in order to investigate them and to better understand the potential of these metal-organic frameworks, it is pertinent to explain how they are made and what their properties are. The explanations of the theory behind MOFs and the respective methods of characterising them will be narrowed, for more detailed explanations see the appropriate appendix section.

1.2.1 Introduction to metal-organic frameworks

The study of metal-organic frameworks (MOFs) has its own branch. These compounds are defined as coordinated networks that contain potential voids with an open framework [15]. Typically they consist of a metal with other atoms connected to it called ligands [13]. The study of these coordinated networks is called reticular chemistry ("reticular" is a term that means "having the form of a net" and is derived from the Latin word "reticulum" meaning "little net").

Metal-organic frameworks are nano-scale porous compounds with large inner surface area. The making of a MOF is done by combining organic compounds and inorganic material. The organic compound's functions as a "linker" by linking together the inorganic material which are "nodes" of metal clusters. These nodes are also known as secondary building units (SBU) [14]. By synthesising MOFs, we can make porous crystal structures that are easy to tune. Once the synthesis of a metal cluster is discovered it can be reproduced with different kinds of linkers [7]. The organic compound determines pore size, also its surface chemistry can be tuned by the vast variety of functional groups organic chemistry has. Functional groups that could be added for tuning the outer and inner surface of a MOF: $-NH_2$, $-F$, $-Cl$, $-COOH$, $-H$, $-Br$, $-I$, $-NO_2$. Also, post synthetic modifications are possible [16].

Many thousands of different MOFs have been discovered, see image 1 [18]. But most are not stable in water, and so far MOFs have a large body of work in their use for gas separation [21][22][23]. Conveniently zirconium based MOFs discovered in Norway have for instance been found to be stable in water [7]. The zirconium based MOF series UiO-66-X (where UiO is an abbreviation of Universitetet i Oslo, and the letter X represents discrete functional groups) was first reported in 2008 by Lillerud and colleagues [7]. With the discovery of water-stable MOFs, the interest in adsorption in liquid media has increased. So far most work in this area has focused on the removal of heavy metals [24][25][26]. It is of more recent and current interest to use MOFs for adsorption of alkali metals, particularly lithium [27][28][29].
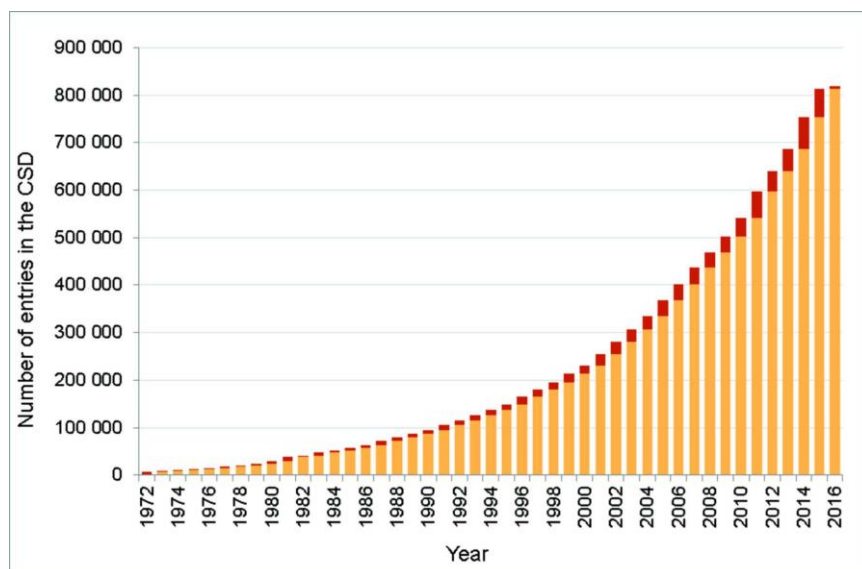

Figure 1. Graph of MOF discoveries in the Cambridge Structural Database (CSD) [18].

2. Project goal

The goal of this project is to test zirconium based MOFs with linkers that have free carboxylate(s) as functional groups. The aim is to use the MOFs as adsorbents where ion exchange will take place between the adsorbent and the adsorbate. That is a proton (H^+) from the carboxylate functional group will be exchanged with a metal ion (Li^+ or Mg^{2+}) from the simulated brine water.

2.1 The zirconium metal cluster node

The choice of MOFs with a zirconium cluster is due to its stability in water [17]. Zirconium based MOFs possess very favourable properties as these MOFs have been found to also display exceptionally good thermal and chemical stability [8]. While Zr-MOFs have great potential, they are yet to be applied into the industry as their synthesis typically is carried out in solvents that are dangerous – one such solvent is N,N-dimethylformamide; it is flammable, toxic and can damage the unborn child [9]. Interestingly it has been reported functionalised Zr-MOFs synthesised with water as solvent [10]. It has also been proposed Zr-MOFs that could be employed under large-scale industrial conditions [8]. The suitability of the Zr-MOF series along with the possibility of industrialised green synthesis has presented a great opportunity to explore lithium uptake using Zr-based MOFs as adsorbent.

MOFs function in different ways, and it's possible for more than one mechanism to take place at a time. In metal adsorption, the different mechanisms can be diffusion, ion exchange, electrostatic interactions, van der Waals forces, hydrogen bonding, Lewis acid-base, chelation, and coordination. In this thesis ion-exchange is of particular interest. The idea is to use carboxylic groups as functional groups on the linkers and see if the free carboxylic groups (COO^-) and the metal ions in the water solution, lithium (Li^+) or magnesium (Mg^{2+}), will chemically bond. For this to happen ion exchange must take place between the proton on the carboxylic group and the metal ions in the solution. This tuning could give the desired selectivity for metal ions. Lithium production can possibly be made more efficient if lithium can selectively be adsorbed from brine, or if magnesium can selectively be separated from the brine.

The two MOFs will differ in their crystal structure, where UiO-66-BDC-COOH will have a fcu-topology typical of UiO-66 MOFs. The Zr-BDC-(COOH)$_2$ on the other hand will have a bcu-topology due to sulphate ions occupying the equatorial plane of the Zr_6-cluster, resulting in an eightfold cell structure as opposed to the twelvefold cell structure of fcu UiO-66-BDC-COOH [8]. A higher number of ion exchange sites should yield greater potential for adsorption. This expectation remains to be analysed. The goal then of this thesis is to successfully synthesise and characterise UiO-66-BDC-COOH and Zr-BDC-(COOH)$_2$, for to then employ these in batch adsorption studies for metal uptake of solutions containing lithium- or magnesium ions. The characterisation is determined by examining crystallinity, thermal stability, porosity, elemental composition, and particle size. Adsorption uptake is determined through batch adsorption experiments with five different concentrations for each metal ion.
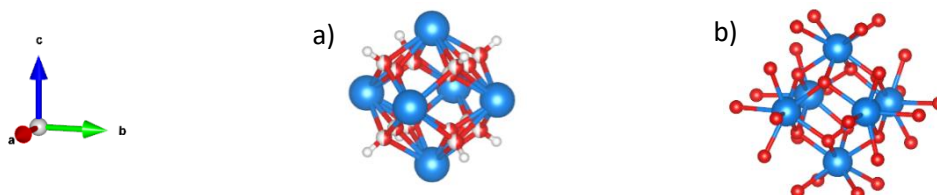
Figure 2. a) Metal cluster of Zr-MOFs UiO-66-BDC-COOH [19], and b) UiO-66-(COOH)$_2$ [8]. Colour representation of atoms: Zr in blue; O in red; and H in wite.

2.2 The formation of the Zr-cluster using HSAB theory

The formation of the zirconium cluster SBU can be explained using the method hard-soft acid-base (HSAB) concept, devised by R. G. Pearson [32]. Categorising acids and bases as either "hard" or "soft" have shown that a general trend where the softer acid pairs with the softer base, and the harder acid pairs with the harder base. According to HSAB theory zirconium is considered a hard acid, characterised as such due to its high charge density (Zr^{4+}), meanwhile, oxygen and hydroxide are considered hard bases. Therewith using HSAB theory the Zr-cluster is expected to form, and indeed do so. Moreover, group four elements interact strongly with oxygen [17]. Zr-MOFs have shown outstanding mechanical stabilities, especially shear stress resistance [33]. The strong metal-ligand bonds in the metal cluster make the structure thermodynamically stable. However, when considering the UiO series experimental results have shown that increasing the linker length causes the stability to decrease. This decrease in stability can be explained by kinetic stability being compromised by the linker compound being less rigid [34].
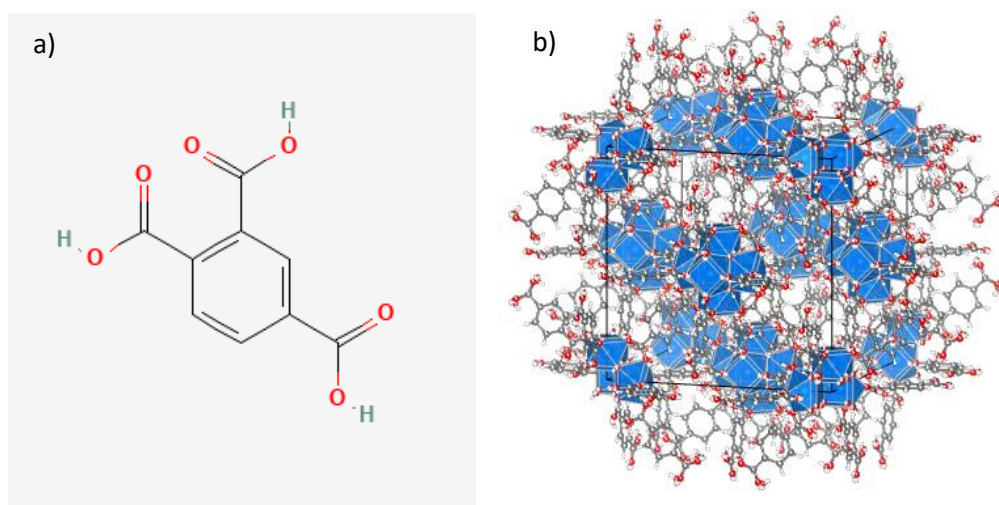
Figure 3. a) Linker: 1,2,4-Benzenetricarboxylic acid (BDC-COOH); common name – trimellitic acid; [35]. b) Unit cell (fcc) UiO-66-Zr-BDC-COOH [19].
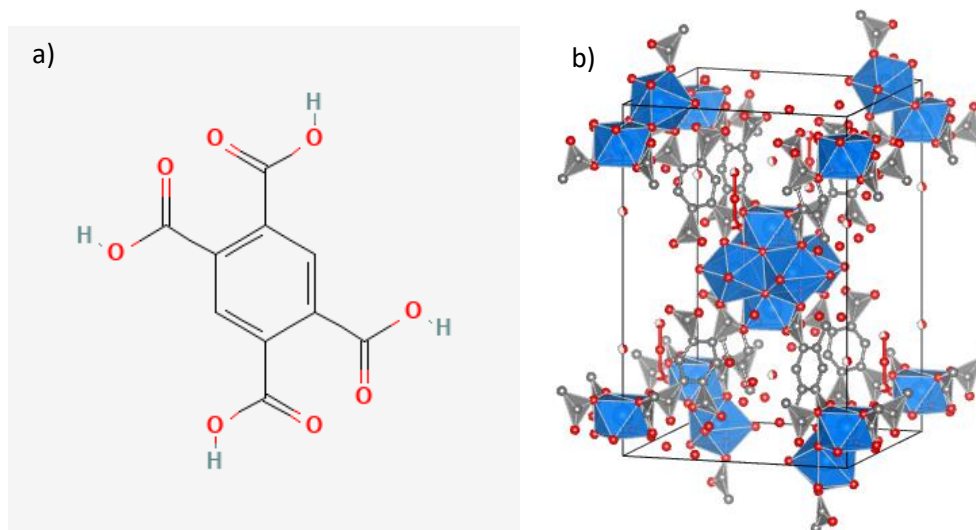
Figure 4. a) Linker: 1,2,4,5-Benzenetetracarboxylic acid (BDC-(COOH)$_2$); common name – pyromellitic acid; [36]. b) Unit cell (bcc) Zr-BDC-(COOH)$_2$ [8].

3. Materials and methods

3.1 Synthesis of MOFs

The procedure for synthesis was to add the reactants to a round-bottomed flask, mix, and then heat with a hot plate. A condenser was attached to the round-bottomed flask for reflux heating, and a magnetic stirrer was used for mixing the solution. All syntheses were carried out in a fume closet. After synthesis the mix was filtered by vacuum and washed with water – if necessary also acetone was used for washing as drying could take quite long. After filtration the product was left to dry in the fume hood.

A goal of the synthesis of these MOFs is to be environmentally friendly, and easy to scale up. For this reason the procedure and reactants for synthesis of the metal-organic frameworks was based on procedures and chemicals found in the article "Green synthesis of zirconium-MOFs†" by Reinsch et al. [8], and from the patent "Process for preparing a zirconium-based metal organic framework" by Reinsch et al. [31]. Where the synthesis for UiO-66-BDC-COOH is based on the patent and synthesis of Zr-BDC-(COOH)$_2$ is based on the article.

Every synthesis used zirconium(IV) sulphate (Zr(SO$_4$)$_2$·4H$_2$O) as source for nodes in the MOF structure, meanwhile different organic compounds were used as sources for linker. Trimellitic acid (1,2,4-Benzenetricarboxylic acid) was used to make UiO-66-BDC-COOH. Pyromellitic acid (1,2,4,5-Benzenetetracarboxylic acid) was used to make UiO-Zr-BDC-(COOH)$_2$. The solvent used in all syntheses was distilled water (H$_2$O) from the university laboratory. Sulfuric acid (H$_2$SO$_4$) was added as modulator to a few syntheses. All chemicals were used as acquired. In total eleven syntheses were performed. Some conditions were changed to observe the effect of the change, such as duration of synthesis or metal to linker ratio. Additionally, scale up synthesis was carried out for the samples with conditions yielding the best results. More detailed tables of each synthesis can be found in the appendix, section B.1.

List of chemicals and where they were purchased from:

(1) Zirconium(IV) sulphate (Zr(SO$_4$)$_2$·4H$_2$O) was purchased from Sigma-Aldrich
(2) 1,2,4-Benzenetricarboxylic acid (BDC-COOH) was purchased from Thermo Scientific
(3) 1,2,4,5-Benzenetetracarboxylic acid (BDC-(COOH)$_2$) was purchased from Sigma-Aldrich
(4) Distilled water (H$_2$O) was acquired from the university laboratory.
(5) Ionised water (H$_2$O) was acquired from the university laboratory.
(6) Sulfuric acid (H$_2$SO$_4$) was acquired from the university laboratory.

3.1.2 Description of syntheses

For the synthesis of sample JA00 (Zr$_6$(OH)$_4$(O)$_4$(BDC-COOH)$_6$·xH$_2$O), 1.0 g of zirconium(IV) sulphate was dissolved in 5.0 ml distilled water while stirring. Once clear solution was obtained 1.0 g of trimellitic acid was added. Another additional 2 mL of distilled water was added to clear the top of the round bottom flask. This reaction mixture was placed on a hot plate which was set to 98 °C, and kept stirring for 1 hour at 98 ± 2 °C. The resulting white solid was separated by vacuum filtration, washed with water, and then dried in air inside a fume hood. The product yield for this synthesis was 1.0131 g, see table JA00 in appendix for more details.

A pH-strip dipped into the solution after zirconium sulfate was dissolved showed a pH value of 0.5. After adding the linker, which is also an acid, the pH was again checked with a pH-strip and the value unsurprisingly was again about 0.5. By adding several acids to water the solution becomes quite acidic, indeed the pH-measurements of solutions after adding the compounds and mixing was 0.5 or lower,

see image 1. For a more detailed overview of synthesis conditions and reaction composition see table 3.
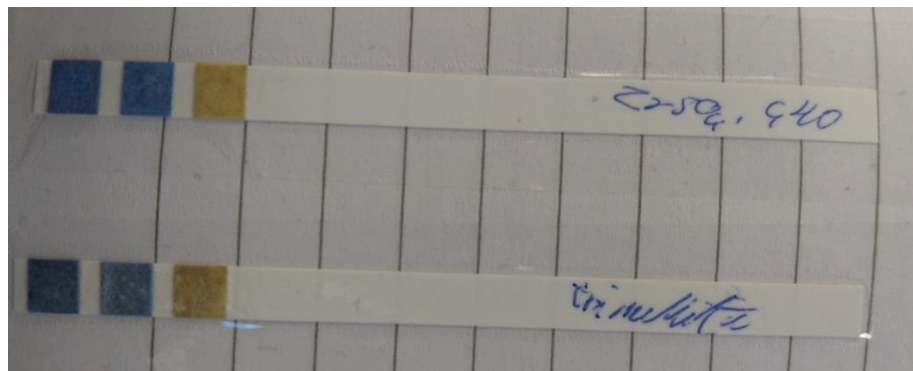
Image 1. pH-strips from measuring pH of sample JA00.

Sample ID	Zr (molequiv)	BDC (molequiv)	Solvent	Modulator (molequiv)	Conditions
JA00	1.0 g (1)	COOH, 1.0 g (1.7)	Water, 7 mL	-	98 °C, 1 h
JA01	0.5 g (1)	COOH, 1.2 g (4)	Water, 7 mL	-	98 °C, 75 min
JA02	1.0 g (1)	$(COOH)_2$, 1.2 g (1.7)	Water, 8 mL	-	90 °C, 2 h
JA03	1.0 g (1)	$(COOH)_2$, 1.2 g (1.7)	Water, 8 mL	-	90 °C, 17 h 45 min
JA04	1.0 g (1)	$(COOH)_2$, 0.5 g (0.67)	Water, 7 mL	H_2SO_4, 0.14 mL (0.95)	90 °C, 18 h 17 min
JA05	1.0 g (1)	$(COOH)_2$, 0.5 g (0.67)	Water, 7 mL	-	90 °C, 17 h 13 min
JA06	3.0 g (1)	COOH, 7.1 g (4)	Water, 50 mL	-	98 °C, 1 h
JA07	5.0 g (1)	$(COOH)_2$, 2.4 g (0.67)	Water, 27 mL	-	90 °C, 18 h 55 min
JA08	5.0 g (1)	$(COOH)_2$, 2.4 g (0.67)	Water, 27 mL	H_2SO_4, 0.4 mL (0.95)	90 °C, 22 h 45 min
JA09	2.0 g (1)	COOH, 5.35 g (4.5)	Water, 48 mL	-	98 °C, 4 h
JA10	3.0 g (1)	$(COOH)_2$, 1.44 g (0.67)	Water, 17 mL	H_2SO_4, 0.24 mL (0.95)	90 °C, 23 h 20 min

Table 3. All syntheses performed. Note: temperature may fluctuate ±2 °C.

3.1.3 Washing and filtration procedure
After synthesis the mixture was left to cool down for a bit. Once cooled the product was filtered and washed. This procedure was done with via vacuum and a büchner funnel. Most samples were washed with only water, but the upscaled batches took so long to dry that some acetone was used in washing the samples in order to make them dry faster.

3.1.4 Drying and storage
Samples were dried in air under ambient atmosphere or in an oven at 70 °C, and stored in a fume hood before being collected in glass sample holders. These were then put into glass vials and placed inside a designated cardboard box.

3.2 Methods of measuring MOF-characteristics

3.2.1 Powder x-ray diffraction (PXRD)

Powder X-ray diffraction (PXRD) analysis was carried using D8 Advance from Bruker with a radiation source of Cu-Kα (wavelength = 0.15418 nm). The samples were finely grounded by mortar and pestle and placed on the sample holder (PMMA, 8.5 mm height, sample reception Ø 25 mm). A thin glass plate and razor was used to pack the sample and smoothen the surface of the powder. The X-ray tube was energized at 40 kV with a current of 25 mA. The samples were scanned from 2° to 70° 2θ with step of 0.0103° and a scan speed of 5.85°/min. The data was exported as XY-files and plotted in excel or qtiplots.

The sample was prepared by grinding the powder into finer granules with a mortar and pestle. This is to improve on the sample texture, more crystals mean more accurate average. After filling the sample holder with sample powder, a microscope slide was used to flatten the top and to fill any gaps. The sample needs to be properly level to avoid peaks at wrong positions, compromised peak shapes, and incorrect intensities.
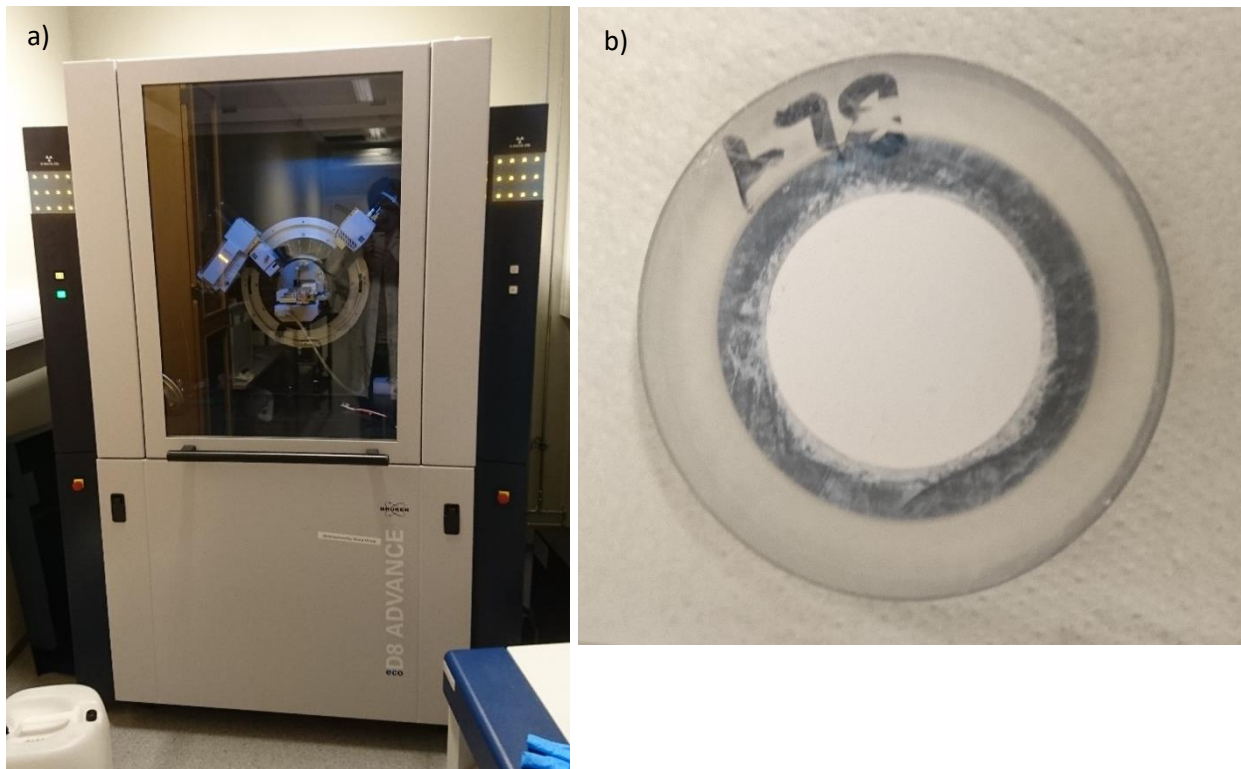
Image 1. a) Instrument for PXRD, Bruker D8 ADVANCE ECO, and b) sample holder with thin film layer.

3.2.2 Thermogravimetric analysis (TGA)

The method of thermogravimetric analysis was static DSC measurement. The instrument used was TGA/DSC 3+ Star system, by Mettler Toledo. Alumina 70ul crucibles were used as sample holders, where circa 20 mg of sample was added and then heated. The surface of the sample in the crucible was flattened by gently tapping the crucible on a table, using a pincer to hold said crucible. The same method was employed for each measurement. The temperature started at 25 °C (room temperature) and heating went on till 800 °C, at a rate of 5 K (5 °C) per minute. The simulated atmosphere consisted of synthetic air and entered the furnace at a flow rate of 20 mL per minute. The data was exported as XY-files and plotted in excel.

Sample ID	Weight before (mg)	Weight after (mg)	Difference weight (mg)
JA00	20.51	6.19	14.32
JA01	21.53	6.11	15.42
JA02	18.90	4.26	14.64
JA03	21.31	4.35	16.96
JA04	21.14	6.23	14.91
JA05	20.82	6.37	14.45
JA07	20.50	6.66	13.84
JA09	20.31	5.87	14.44

Table 4. Measured weights of samples. Weight loss after TGA measurement.

Image 2. Residual sample after TGA-measurement.

3.2.3 Nitrogen (N₂) adsorption

Nitrogen adsorption was measured using a Micromeritics® TriStar II Plus. For gas adsorption isotherms, high-purity grade (99.999%) nitrogen (N_2) was used. The data was exported as xy-files and plotted in excel. Before nitrogen adsorption the samples were activated (degassed) by heating at 120 °C under vacuum for 2 hours. The mass of activated sample was calculated by the mass difference of the cell with cap before and after activation. Instrument used for activation was Micromeritics VacPrep 061.

Three marked sample holder vials were prepared for measurement. The vials were cleaned and removed of any chemicals by drying in a heated oven. Each vial was weighed with a lid on. Then samples were added and weighed. The samples each weighed around 120 mg. Before measuring the samples were activated. Activation of MOFs remove solvent. The vials after activation were weighed again and thereafter mounted to the instrument for measuring. The vials during measurement were submerged in liquid nitrogen in order to get the appropriate temperature for measurement, that is $-196\,°C$ or 77 K.
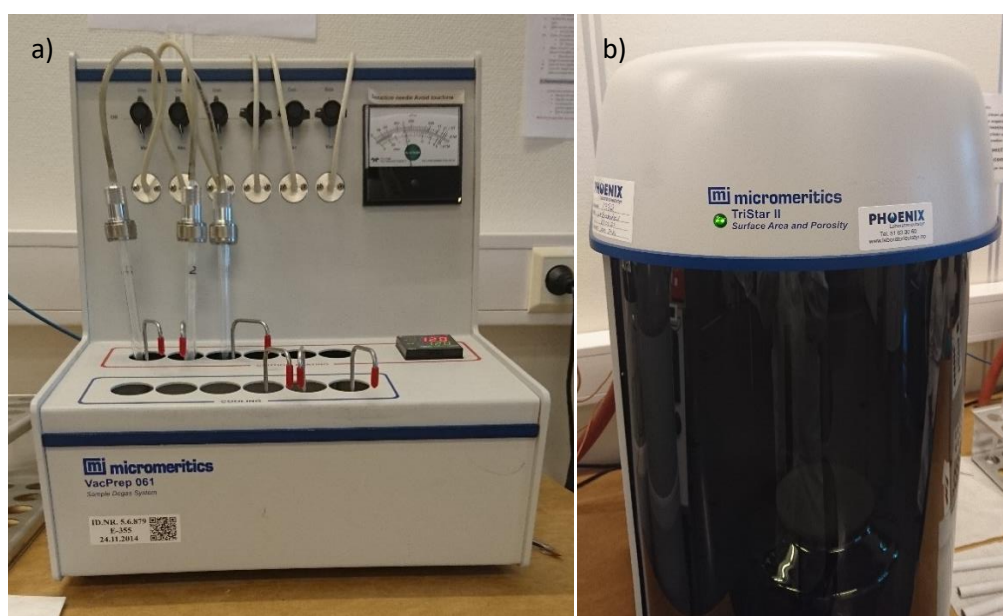
Image 3. a) Instrument for activation, Micromeritics VacPrep 061, and b) instrument for N_2-sorption measurement, Micromeritics® TriStar II Plus.

Sample ID	Weight of sample holder, incl. lid (g)	Sample weight before measurement (mg)	Sample weight after activation (mg)
JA01	28.9361	119.5	90.1
JA04	29.4151	119.2	91.4
JA05	29.1425	122.5	96.6

Table 2. Sample weights of N_2-sorption measurement.

3.2.4 ATR-IR spectroscopy

IR spectra were collected with Agilent Cary 630 ATR-IR Spectrometer. A blank background spectrum was measured before each sample spectrum measurement. The powder samples were grounded by mortar and pestle, and a small portion was placed on top of the diamond. Between each measurement the crystal was wiped with soft paper to clean the surface. The ATR-IR spectra were recorded from 650–4000 cm^{-1} with 32 scan per spectrum. The data was exported as XY-files and plotted in qtiplot.

3.2.5 Scanning electron microscopy (SEM) & energy dispersive x-ray spectrometry (EDS)

The microstructures of the specimens were analyzed with scanning electron microscopy (SEM), Gemini SUPRA 35VP (ZEISS) (Carl Zeiss, Jena, Germany) equipped with EDAX energy dispersive X-ray spectroscopy (EDS).
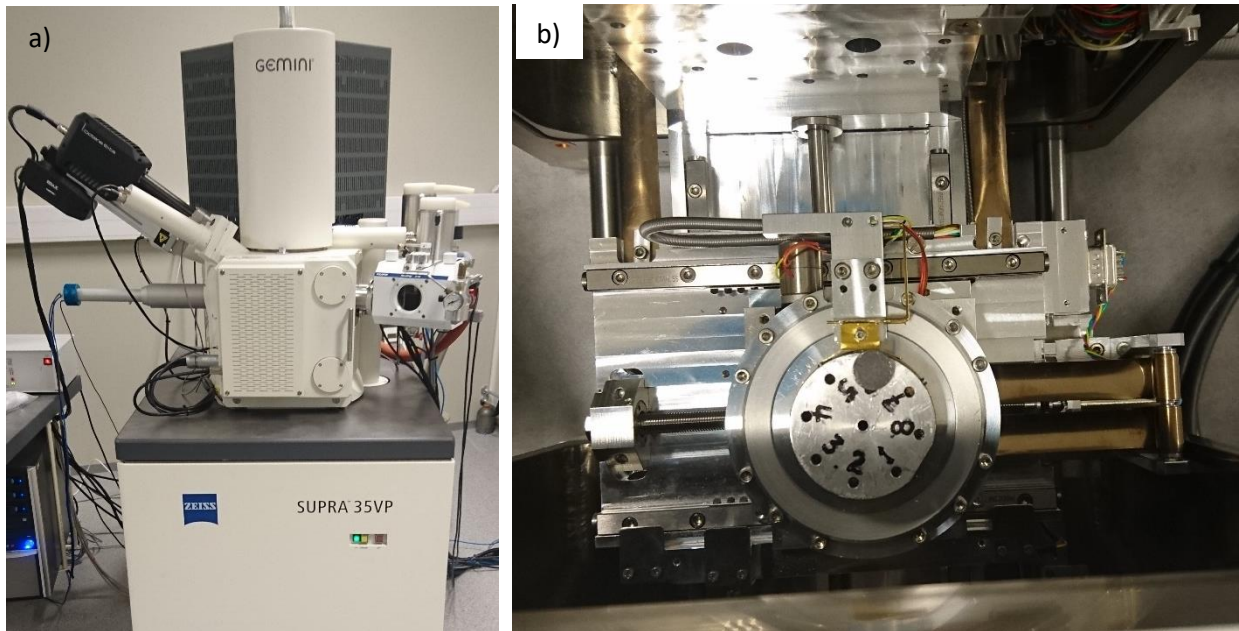
Image 4. a) Instrument used for SEM-EDS measurements and analysis, and b) inside compartment for loading samples.

In order to obtain SEM images, the sample must be electrically conductive at the surface. The sample must also be grounded as to not accumulate charge. The samples were fastened onto the sample holders using carbon tape, also called nano tape (which is a conductive adhesive). The sample were then blasted with palladium, creating a conductive "coat" over the sample surface. Materials that are conductive allow electrons to move inside them – this means that the conductive coating in combination with the carbon tape for grounding, allows the electrons to be directed away and to not accumulate in the sample.
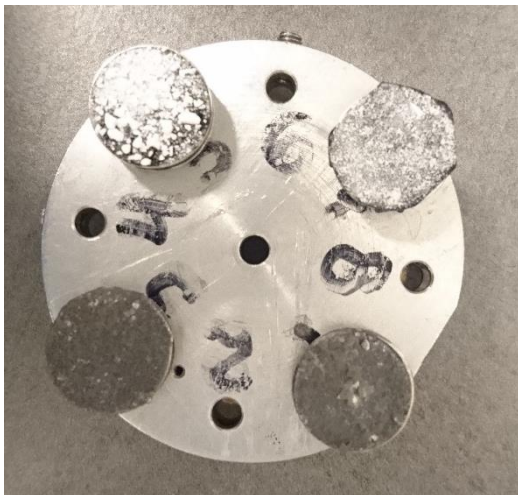
Image 5. Preparation of samples. The two samples placed on 1 and 3 are coated, while the other two samples placed on 5 and 7 are not – all four samples are fastened onto carbon tape.

3.2.6 Inductively coupled plasma optical emission spectroscopy (ICP-OES)

The Perkin Elmer Optima 4300 DV instrument, fitted with a fully demountable 1-slot quartz torch, was used for the analysis (Table 1 in figure 5). The high-energy echelle-based Optima polychromator utilizes one or two Segmented-array Charge-coupled Device (SCD) detectors depending on the Optima model. The measured resolution of the system is 0.006 nm at 200 nm. This instrument is ideal for the analysis of complex matrix samples due to the pre-optimized radial and axial view. The Optima 4300 DV ICP-OES has continuous wavelength coverage from 167 to 852 nm. Combined with the SCD detection of over 6000 × 6000 pixels, this allows the 79 spectral lines per mm.

3.2.6.1 Preparation of the calibration standards

The calibration standards were prepared in 5 vials. A known volume of lithium standard solution with a concentration of 5 mg/L was added and mixed with a known volume of HNO_3 5%. As typically the highest concentration of the lithium in brines are higher than 5 mg/L, the maximum range for calibration standard solution was made by the known concentration of lithium chloride solution. The LiCl solution was prepared by addition of the 0.2 g LiCl salt per 100 mL water corresponding to the highest lithium content in brines. Then three different dilutions 1:50, 1:100, and 1:200 are applied for the LiCl solutions.

Table 1 ICP-OES parameters used for analysis

Parameter	Setting
Instrument model	Perkin Elmer Optima 4300 DV
Observation method	Radial and axial
Plasma torch	1-Slot Demountable Quartz
Injector	Alumina, 2.0 mm i.d.
Spraychamber	Standard glass cyclonic
Nebulizer	MiraMist PEEK
Pump flow rate	1.5 mL/min
Plasma RF power	1400 W
Nebulizer gas flow	0.7 L/min
Auxiliary gas flow	0.5 L/min
Cool gas flow	15 L/min

a)

b)

$y = 120732x + 26981$
$R^2 = 0.998$
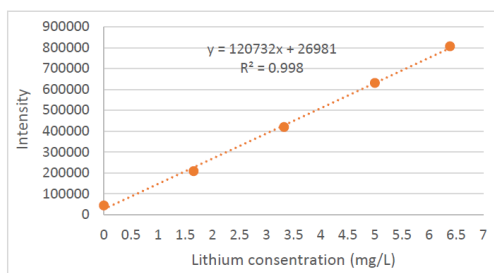
Figure 3 standard calibration curve

Figure 5. a) Table 1 ICP-OES parameters used for analysis, and b) Figure 3 standard calibration curve.

3.2.6.2 Sample preparation

The samples for ICP-OES analysis were filtered through a 0.2 µm PVDF syringe filter before being received at the ICP laboratory (not the ref. samples). Samples and ref.samples were further diluted with 5% HNO_3 prior to analysis.

3.2.7 Batch adsorption study

Batch adsorption was performed to study the ability of the MOFs to take up metal ions. After the MOF samples had gone through the adsorption experiment different methods were employed to find the adsorption effectiveness. In order to find lithium concentration left in the lithium-ion batch solutions ICP-OES was employed, meanwhile magnesium can be detected by EDS so SEM-EDS was employed for the magnesium-ion batch solutions. Solutions also had pH values and conductivities measured in order to look for any trends.

3.2.7.1 Preparation of stock solutions

When making the metal-chloride solutions volumetric flasks were used to dilute the solutions. Chosen volume for the solutions to be used in the metal uptake experiments was 20 mL. Chosen concentration was based on concentrations of lithium in brines (200 – 1400 mg/L) [37]. The calculation was done using both constituents, this however still yielded a concentration within the commercially viable range. The magnesium concentration calculation on the other hand was simply copied of off the lithium calculation.

3.2.7.2 Ion-selective electrode & pH-electrode

Measurements of pH and conductivity were carried out using a multi-parameter meter MU 6100 L. For pH measurement a SenTix® PLUS pH electrode was used. Before measuring the instrument was calibrated using a three point calibration by following instructions from the instrument manual. The conductivity probe CO 11 came with the instrument and was used for measuring conductivity. Before conductivity measurement the probe was checked against two solution of known conductivity. Known conductivites were 64 µS/cm and 210 µS/cm and the probe measured $65.73 \pm 1.13 \, \mu S/cm$ and $216 \pm 0 \, \mu S/cm$ respectively.
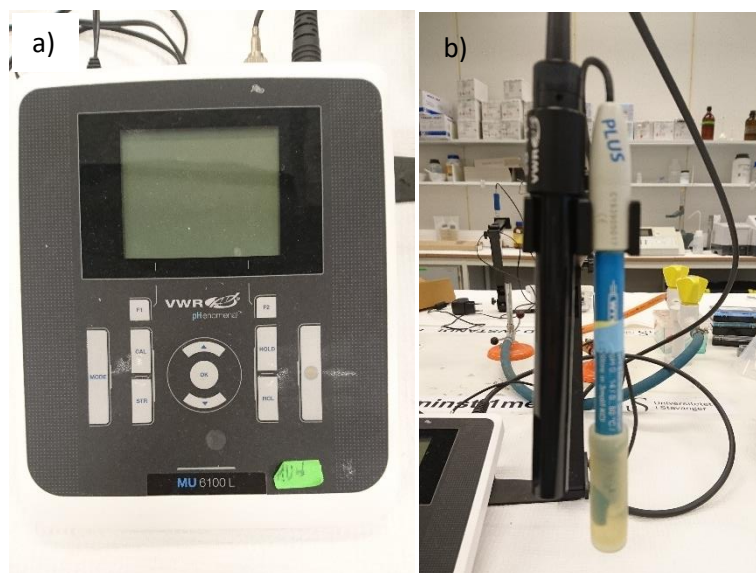
Image 6. a) pH and conductivity measuring instrument, and b) respective electrodes.

3.2.7.3 Preparation of adsorption samples

Samples used in the metal uptake study were JA09 and JA10. Five capped bottles had 20 mL aqueous metal-chloride solution added to it. Thereafter powder MOF samples were added, 100 mg in each bottle. The five bottles were put into a water bath. Each bottle was given a stirrer for mixing the solution and left overnight. Two metal uptake studies were carried out for each MOF. First for uptake of lithium from aqueous lithium chloride solution. Second for uptake of magnesium from magnesium chloride solution. After adsorption the MOF powder was separated by a centrifugation instrument for 15 minutes at 4000 rpm. The liquid solutions were then extracted using syringes and 0.2 µm PVDF syringe filters. The solids was left to dry in an oven at 60 °C for overnight. Concentrations of the solutions before the adsorption experiments were {230,115,57.5,29,14} mg/L Li^+, and {447,357.5,179,89,45,22} mg/L Mg^{2+}.

4. Results and discussion

4.1 Synthesis discussion

Product yield may give an idea of how the synthesis may be optimized for scale-up synthesis. The metal component of the MOF is used as a limiting reactant which means the disparity in theoretical yield and experimental yield can be explained by an excess of the unreacted linker. Naturally also solvent will be contained in the MOFs after synthesis. Fortunately, all samples prepared in this thesis have used water as solvent, hence the term "green"-synthesis. Water is easier to remove from the MOF pores, and it's not toxic or otherwise harmful to the environment. See thermogravimetric analysis (TGA) sections for closer study of the compositions of the MOF samples.

MOF	Sample	Yield [g]	Percent yield	L:M
UiO-66-BDC-COOH	JA00	1.0131	111%	1.7:1
	JA01	0.5303	117%	4:1
	JA06	3.1272	115%	4:1
	JA09	2.2035	121%	4.5:1
Zr-BDC-(COOH)$_2$	JA02	2.5908	286%	1.7:1
	JA03	1.0407	112%	1.7:1
	JA04	0.9716	107%	0.67:1
	JA05	1.0186	112%	0.67:1
	JA07	4.3696	96%	0.67:1
	JA08	-	-	0.67:1
	JA10	2.7273	100%	0.67:1

Table 5. Yield of synthesis of Zr-MOF. Percent yield is calculated using FW of non-solvated MOF. Note: JA08 was contaminated.

For the sake of clarity BDC-COOH will be discussed first, then later discussion of BDC-(COOH)$_2$ will follow. Eleven syntheses in total were carried out. See table 6 for yield – more detailed information can be found in the appendix.

Four syntheses was carried out for UiO-66-COOH. The main difference between samples JA00 and JA01 is the different linker to metal (L:M) ratio being 1.7:1 for JA00 and 4:1 for JA01. Samples JA06 and JA09 were upscaled from JA01 synthesis. Reagent stoichiometry was kept the same, but reaction time (duration of synthesis) was unchanged for JA06, while JA09 was given longer duration, that is one hour and four hours reaction time respectively.

Seven synthesis of Zr-BDC-(COOH)$_2$ were carried out. Effect of addition of modulator (H$_2$SO$_4$) and reaction time was tested. The original synthesis reported by Reinsch et al H$_2$SO$_4$ is added as modulator and the reaction time is sixteen hours. Sample JA04 is a replica of this synthesis. Samples JA02, JA03, and JA05 were synthesised without addition of H$_2$SO$_4$. What's more, JA02 and JA03 had higher linker to metal ratio. Additionally, JA02 had its synthesis duration set to only two hours to compare with JA03 which was left overnight. Even though JA03 produced good product yield, both syntheses showed poor results of crystallinity. See the appendix section B.2 for graph.

Samples JA04 and JA05 differed only in addition of H$_2$SO$_4$, that is JA05 was synthesised without adding modulator. Sample JA04 gave a lower product yield than JA05, though this may not be due to lower residual linker – further discussion follows in the PXRD section below. Although the yields of the syntheses do not show significant difference, the characterization results (discussed below) shows that samples differ significantly.

Samples JA04 and JA05 were chosen for scaleup. The next two syntheses of JA07 and JA10 mirrored the differentiation between JA04 and JA05, where the only difference was one had modulator added to its mixture while the other did not. JA10 had modulator added while JA07 didn't. All the upscaled syntheses were dried in an oven at 70 °C. Sample JA10 gave nigh 100% product yield while JA07 gave less than 100%. Considering the amount of scaleup the samples most likely would have benefitted from an increase in the duration of synthesis by a couple more hours.

4.2 Results of IR

IR performed on the samples JA10, JA04, and JA09 to determine whether the syntheses performed indeed yielded the MOF product that was reported in the patent[31] and the green synthesis article[8]. The results corresponded well with the reported "fingerprint"-graphs. JA09 was also measured after being activated. Its fingerprint was still recognizable – it had not decomposed. The vibrational signature of free functional group (COOH-1750 cm^{-1}) is observed in all samples. The broad peak in the region 2500 – 3500 cm^{-1} indicated hydrogen bonded water physisorbed molecules.

Figure 6. IR results of: a) JA10; b) JA04; c) JA09 (washed); d) JA09 (activated).

4.3 Results of PXRD

PXRD measurements were used as confirmation of successfull synthesis of UiO-66-BDC-COOH and Zr-BDC-(COOH)$_2$. All samples were measured as synthesised. The plot shows intensity versus diffraction angles. The broadness of a diffraction peak corresponds to the mean crystallite size. The smaller the average crystallite size, the broader the reflections and the lower the absolute intensities [38]. Defects in the crystalline structure come about from substituted atoms, structural defects, or from thermal treatment. Defects create strain and strain will broaden the diffraction line [38][39].
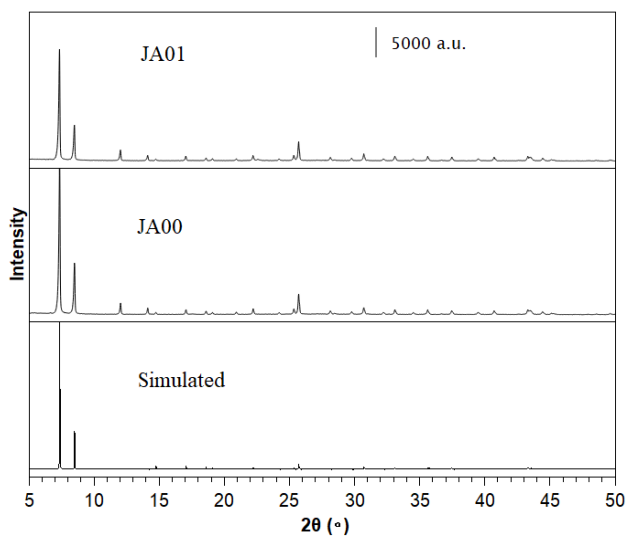
Figure 7. PXRD plots of UiO-66-BDC-COOH, samples were synthesised using different L:M ratios.

Interestingly, JA00 was synthesised with linker to metal ratio on the lower end of what was reported in the patent, 1.7:1 from the range 1:1 to 5:1 that was reported in the Reinsch et al. patent [31]. The linker BDC-COOH is expensive – it costs 2450 NOK per 100 g [40]. If the amount of excess linker can be reduced it would save costs. This is important for upscale synthesis. Sample JA01 only differs from JA00 in its linker to metal ratio. The JA01 4:1 ratio was reproduced from the experiment "synthesis in a round bottom flask" from the patent [31]. Although sample JA00 had lower amount of linker than JA01, it showed more intense and narrow peaks peaks than JA01, suggesting that it produced bigger crystals.

The first attempt at upscale synthesis of JA01 (same molar equivalents), sample JA06, yielded poorly crystalline material. The cause was considered to be due to low reaction time. The second attempt of upscale of JA01, JA09, proved this consideration to be correct as its duration was increased from one to four hours and produced much better results. Indeed, JA09 showed even better results than JA01. By allowing the synthesis to last longer a highly crystalline material is made. However, striking a balance between reaction time and crystallinity of the product is a tentative yet valuable prospect.

Figure 8. PXRD plots of scaleup of JA01.
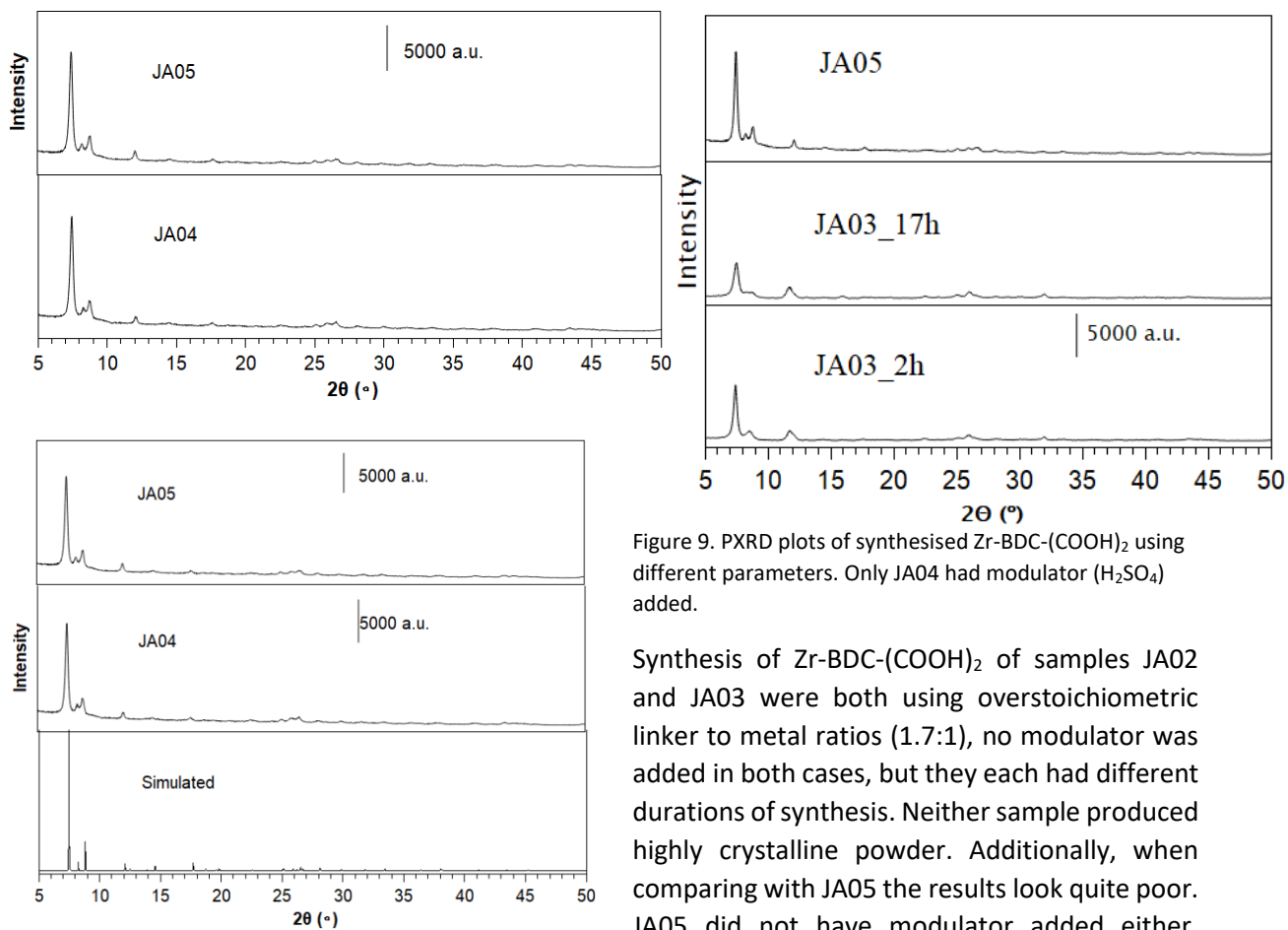
Figure 9. PXRD plots of synthesised Zr-BDC-(COOH)$_2$ using different parameters. Only JA04 had modulator (H$_2$SO$_4$) added.

Synthesis of Zr-BDC-(COOH)$_2$ of samples JA02 and JA03 were both using overstoichiometric linker to metal ratios (1.7:1), no modulator was added in both cases, but they each had different durations of synthesis. Neither sample produced highly crystalline powder. Additionally, when comparing with JA05 the results look quite poor. JA05 did not have modulator added either, though it did have long reaction time like JA03, and used understoichiometric linker to metal ratio. Samples JA04 and JA05 were carried out to compare the effect of adding modulator to the synthesis. Surprisingly, JA05 shows slightly nicer peaks when comparing the first three peaks in the 5 to 10 2θ area of the graph. JA04 and JA05 when comparing with the simulated PXRD pattern confirms Zr-BDC-(COOH)$_2$ was successfully synthesised.
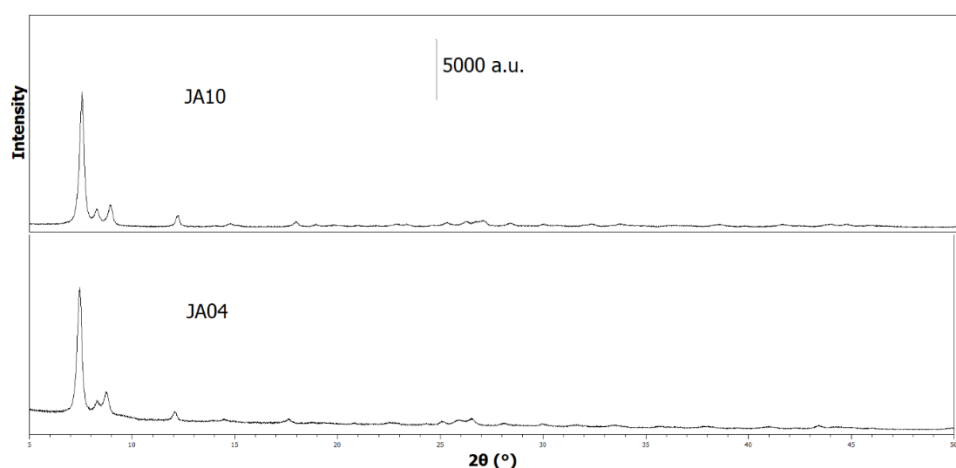
Figure 10. Comparing PXRD results of JA04 and JA10.

Sample JA10 was an upscaled synthesis based on JA04. JA10 also had a few hours prolonged synthesis duration – 23 hours and 20 mintues. The increased duration yielded even better crystallinity than the downscaled sample. There was also an upscaled synthesis of JA05 – JA07 – but this sample had poor crystallinity, see appendix section B.2 for figure.

4.4 Results of TGA

The TGA-plot shows the rise in temperature in the x-axis, while the y-axis show weight percentage, where the final weight is considered 100 wt% of ZrO_2. The solid blue line shows a decrease in weight as the sample is heated. A stipulated red line shows where the MOF should start to decompose based on the ideal composition of the MOF. Decomposition involves several steps. After synthesis and washing, the MOF structure will contain solvent, which is in all syntheses in this thesis water, and is considered *wet*. By heating the sample, the solvent is removed, and the sample is considered *dried*. Further heating removes OH-bonds, this step is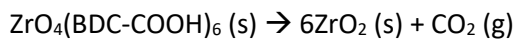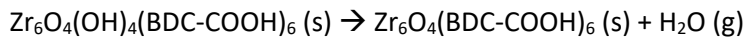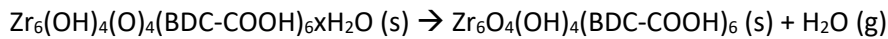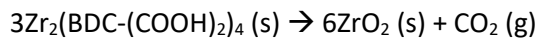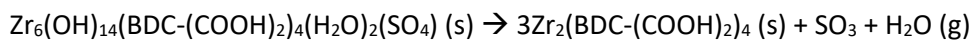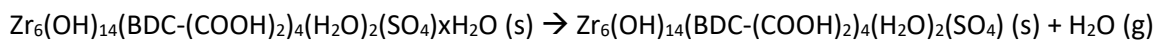 called *dehydroxylation*. The removal – desorption – of solvent and OH-bonds require energy and is therefore endothermic processes. The last step however is exothermic as material no longer can absorb heat and the bonds in the MOF structure break. The ideal MOF calculation equations can be found in the appendix. Also, there is a grey dotted line in the plot showing the heat flow.

4.4.1 Decomposition calculations

For samples JA00, JA01 and JA09 the decomposition would follow the following steps:

$Zr_6(OH)_4(O)_4(BDC\text{-}COOH)_6xH_2O$ (s) $\rightarrow$ $Zr_6O_4(OH)_4(BDC\text{-}COOH)_6$ (s) + H_2O (g)

$Zr_6O_4(OH)_4(BDC\text{-}COOH)_6$ (s) $\rightarrow$ $Zr_6O_4(BDC\text{-}COOH)_6$ (s) + H_2O (g)

$ZrO_4(BDC\text{-}COOH)_6$ (s) $\rightarrow$ $6ZrO_2$ (s) + CO_2 (g)

For samples JA02, JA03, JA04, JA05, JA07 and JA10 the decomposition would follow the following steps:

$Zr_6(OH)_{14}(BDC\text{-}(COOH)_2)_4(H_2O)_2(SO_4)xH_2O$ (s) $\rightarrow$ $Zr_6(OH)_{14}(BDC\text{-}(COOH)_2)_4(H_2O)_2(SO_4)$ (s) + H_2O (g)

$Zr_6(OH)_{14}(BDC\text{-}(COOH)_2)_4(H_2O)_2(SO_4)$ (s) $\rightarrow$ $3Zr_2(BDC\text{-}(COOH)_2)_4$ (s) + SO_3 + H_2O (g)

$3Zr_2(BDC\text{-}(COOH)_2)_4$ (s) $\rightarrow$ $6ZrO_2$ (s) + CO_2 (g)

Reaction equation of the decomposition*:

$Zr_6O_4(OH)_4(C_9H_6O_6)_6$ (s) + O_2 (g) $\rightarrow$ $6ZrO_2$ (s) + $9CO_2$ (g) + H_2O (g)

$Zr_6(OH)_{14}(C_{10}H_6O_8)_4(H_2O)_2(SO_4)$ (s) + O_2 (g) $\rightarrow$ $6ZrO_2$ (s) + $10CO_2$ (g) + SO_2 (g) + H_2O (g)
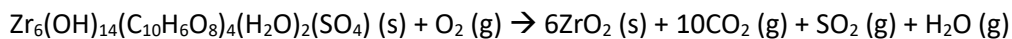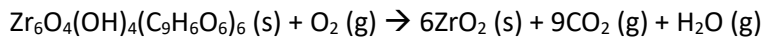
* Equations are not balanced. Oxygen (synthetic air) is introduced into the furnace during heating.

Ratio of molecular mass for ideal MOF of each structure (1):

$$\frac{FW_{MOF}}{6FW_{ZrO_2}} = FW_{ratio\frac{MOF}{ZrO_2}}$$

In equation 1 the formula weight of a zirconium-MOF, FW_{MOF}, is divided by six times the zirconium oxide, $6FW_{ZrO2}$, that is the end product of the thermal treatment from the TGA. One formula unit of MOF consists of six zirconium, that is why the zirconium oxide is multiplied by six. This equation gives the ratio of the weight of each MOF molecule to six zirconium oxides. The equation is based on the presumption that the molecules are ideal, that is they are without contaminants or structural defects. With this calculation TGA plots are normalised by setting the end product, ideal zirconium oxide, to 100% wt% and setting the MOF wt% to the *FWratio*, which should give the ideal MOF before the thermal treatment.

The FW of UiO-66-BDC-COOH when it is dry is 1940.18 g/mol while ZrO_2 is 123.222 g/mol. Zr-BDC-$(COOH)_2$ on the other hand can have different structures which means different FW. With this in mind, three different FW were used in calculating ideal MOF, see table 6. Calculation of ideal MOF using

equation 1 gave the following FWratios 2.62 for UiO-66-BDC-COOH, and 2.39, 2.55, and 2.47 for Zr-BDC-$(COOH)_2$. For more details see table 7.

Atom	FW	#1 COOH	#1 $(COOH)_2$	#2 $(COOH)_2$	#3 $(COOH)_2$
Zirconium	91.22	6	6	6	6
Oxygen	16	44	44	48	46
Carbon	12.01	54	40	40	40
Hydrogen	1.008	40	32	28	30
Sulphate	32.07	0	0	2	1
FW		1940.18	1763.984	1888.092	1826.038

Table 6. The FW of each possible MOF structure has been calculated adding together the FW of each element present in the structure. Zr-BDC-$(COOH)_2$ has structures $Zr_6(O)_4(OH)_4(L)_4(OH)_4xH_2O$ (#1), $Zr_6(O)_4(OH)_4(L)_4(SO_4)_2xH_2O$ (#2), and $Zr_6(O)_4(OH)_4(L)_4(OH)_2(SO_4)xH_2O$ (#3). L represents linker.

MOF	Samples	Wi (mg)	Wf (mg)	Δm (mg)	FWratio
UiO-66-BDC-COOH	JA00	20.51	6.19	14.32	262%
	JA01	21.53	6.11	15.42	
	JA06	-	-	-	
	JA09	20.31	5.87	14.44	
Zr-BDC-$(COOH)_2$	JA02	18.9	4.26	14.64	239% (#1)
	JA03	21.31	4.35	16.96	255% (#2)
	JA04	21.14	6.23	14.91	247% (#3)
	JA05	20.82	6.37	14.45	
	JA07	20.5	6.66	13.84	
	JA08	-	-	-	
	JA10	20.37	6.42949	13.94	

Table 7. Weight loss of samples after TGA, as well as ideal MOF calculated using equation 2 from the appendix.
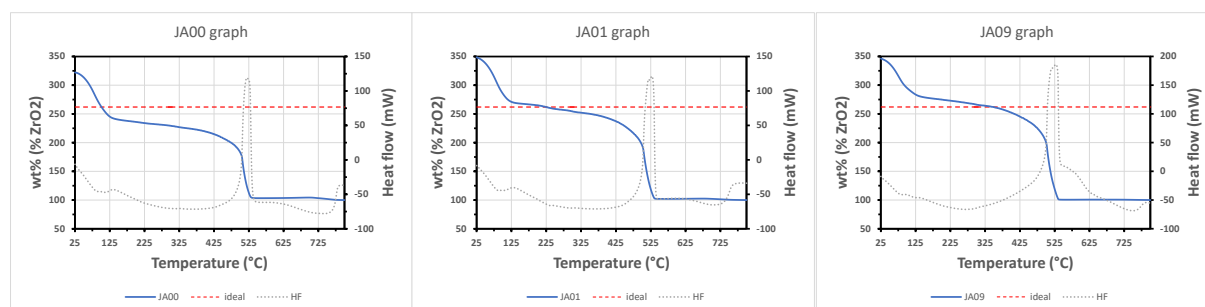
Figure 11. Samples JA00, JA01, and JA09. Ideal MOF would start to decompose at 262 wt%.

The first change in mass is due to water evaporating as the sample is dried (50 – 120 °C). This water is physisorbed by the MOF which means when it evaporates the pores are freed up. Following the dry sample is a continued decrease of mass (120 – 300 °C), this part is called dehydroxylation as hydroxides that has been chemically bonded in the MOF structure is released as water vapour. The structural stability of the MOF is not compromised by the dehydroxylation step. The measurement of sample JA01, see figure 11, does not show a flat line, which is what would indicate what its thermal stability is, instead it's always decreasing, though it's not a steep decline until around 400 °C. At 400 °C and up the MOF is definitely collapsing. These transitions apply to both UiO-66-BDC-COOH and Zr-BDC-$(COOH)_2$ samples, but not all samples may fit into this story. Particularly samples JA02 and JA03 have a lot of mass loss before the MOF structure starts to decompose. Furthermore, their heat flow lines in the graph have strange trajectories.

Comparing samples JA00 and JA01 shows a significant difference in when the MOF starts to decompose taking into account ideal MOF decomposition starts at 262 wt%. A probable cause for this is that due to the low linker to metal ratio in sample JA00 it contains more defects; hence its decomposition starts at a lower wt%. Meanwhile, sample JA09 seems to have a composition close to the ideal MOF, granted this synthesis had longer duration and slightly greater L:M ratio. Although the JA09 synthesis was upscaled this finding suggests increased duration yields more crystal formation.
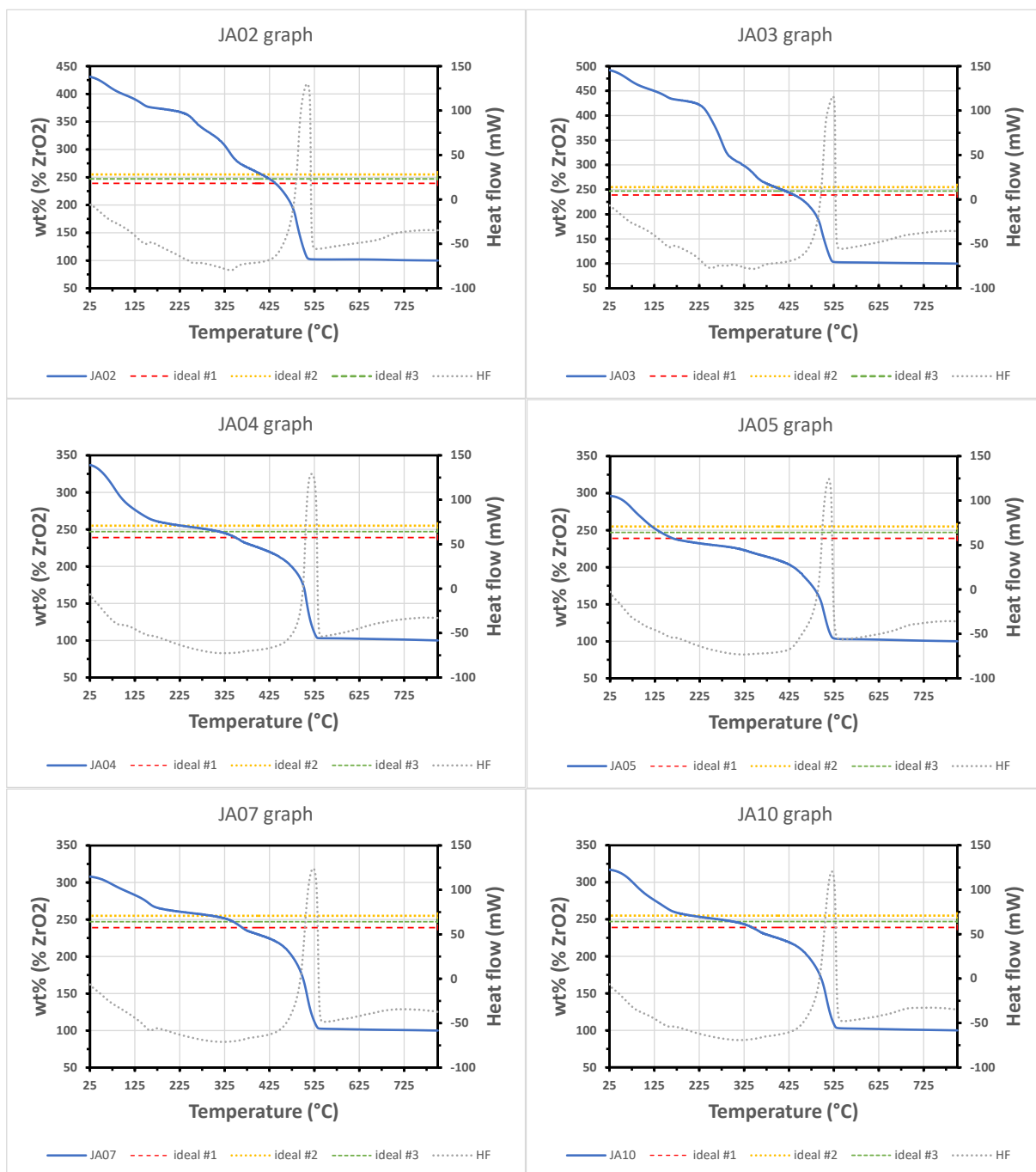
Figure 12. Samples JA02, JA03, JA04, JA05, JA07, JA10. Ideal MOF would start to decompose at 239, 247 or 255 wt%.

Samples JA02 and JA03 had higher linker to metal ratio than the other Zr-BDC-(COOH)$_2$ syntheses, but produced very poor crystallinity, see PXRD graph in the previous section. They show a strange heat flow and significant mass loss via desorption before the MOF decomposition temperature. It is possible that the mass loss is due to residual linker or structural defects. The difference between JA04 and JA05 is quite significant in that JA05 is already decomposing at 120 °C. This can be explained by structural

defects which suggests the addition of modulator in JA04's synthesis assisted in formation of MOFs. Modulator may be significantly advantageous in preventing defects. Sample JA07 was upscaled JA05 yet shows improved thermal stability. This is surprising because JA07 had uncompelling PXRD result, see appendix section B.2. Sample JA10 gave expectedly similar result as JA04 – good thermal stability.

4.5 Results of N_2-sorption

4.5.1 Isotherm plots
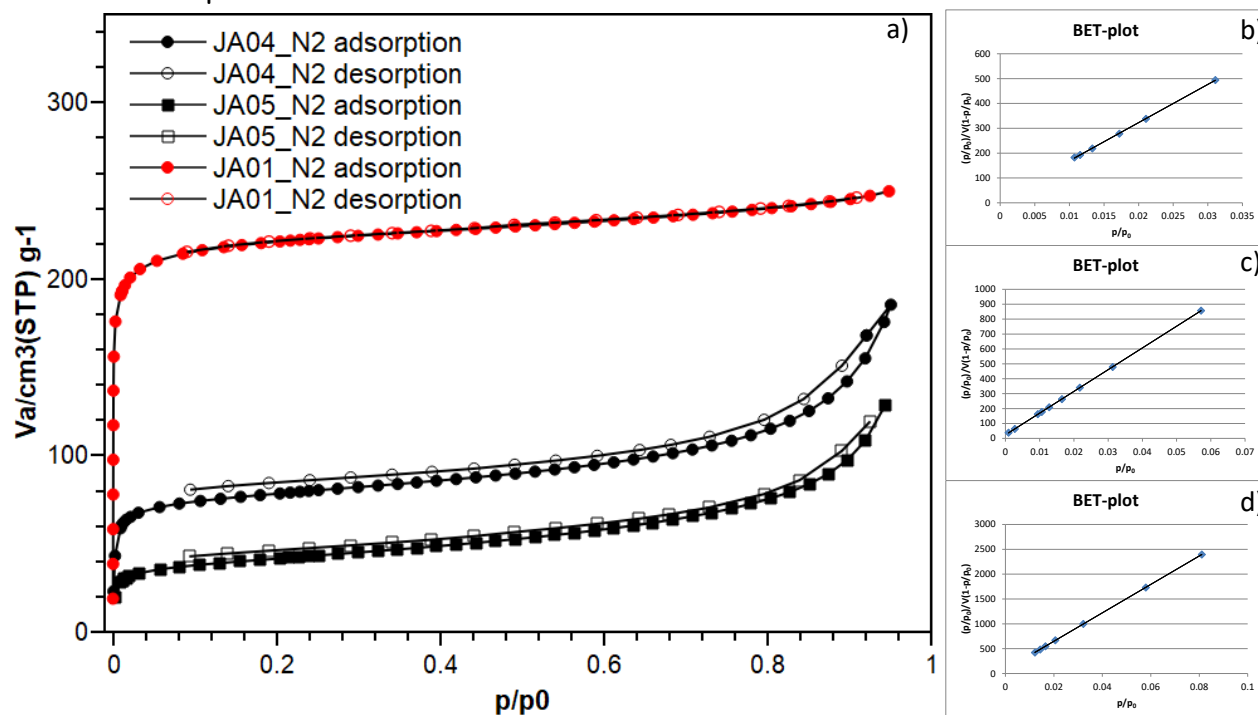
Figure 13. a) Nitrogen adsorption plot, b) JA01 BET-plot, c) JA04 BET-plot, and d) JA05 BET-plot.

Sample ID	MOF type	C values (error %)	V_M values (error %)	BET values (error %)	Total Pore Volume	Startpoint - endpoint
JA01	UiO-66-Zr-BDC-COOH	2041 (8.3%)	201 (0.2%)	874 (0.2%)	0.333 – 0.356 (6.3% diff.)	6 – 16
JA04	UiO-66-Zr-BDC-(COOH)$_2$	604 (2.2%)	69 (0.1%)	298 (0.1%)	0.125 – 0.125	1 – 9
JA05	UiO-66-Zr-BDC-(COOH)$_2$	370 (2.1%)	35 (0.1%)	152 (0.1%)	0.066 – 0.066	3 – 9

Table 8. Data from N_2-sorption measurement.

Comparing results of nitrogen adsorption with the results found in the literature shows good conformity between the isotherm plots. The BET values also closely coincide, indeed results gave slightly higher surface area than the literature. One exception is JA05. Likely this sample has a large amount of defects in its structure. In fact, after activating JA05 at 80 °C its structure had been compromised considerably, see figure 14 b). While JA04 showed good conformity with the literature, it still had loss of structure after activation, see figure 14 a). Sample JA01 on the other hand showed excellent stability.
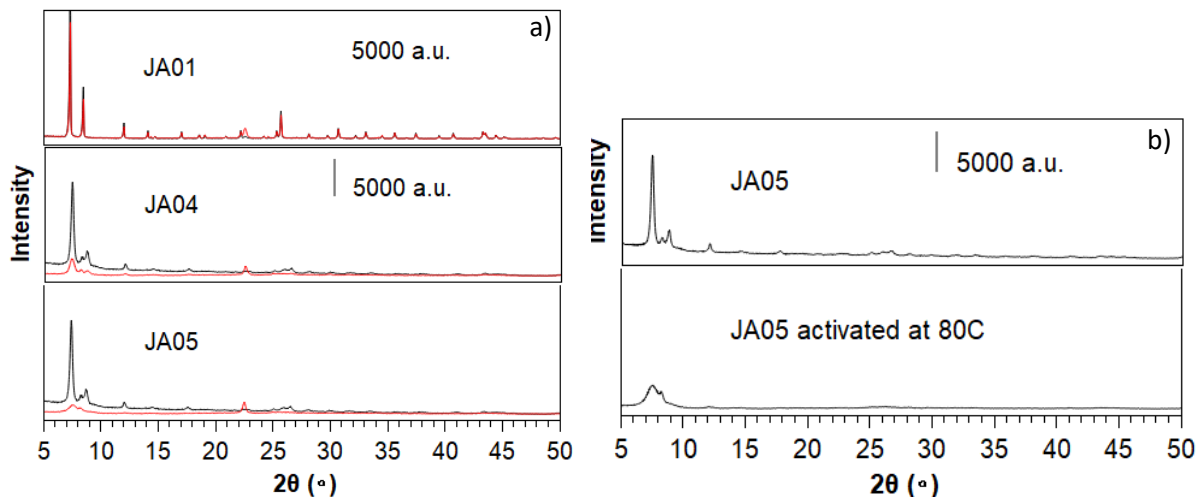
Figure 14. a) Before (black) and after (red) N$_2$-sorption, b) sample JA05 was activated in air, but collapsed at 80 degrees

4.6 Results of SEM-EDS
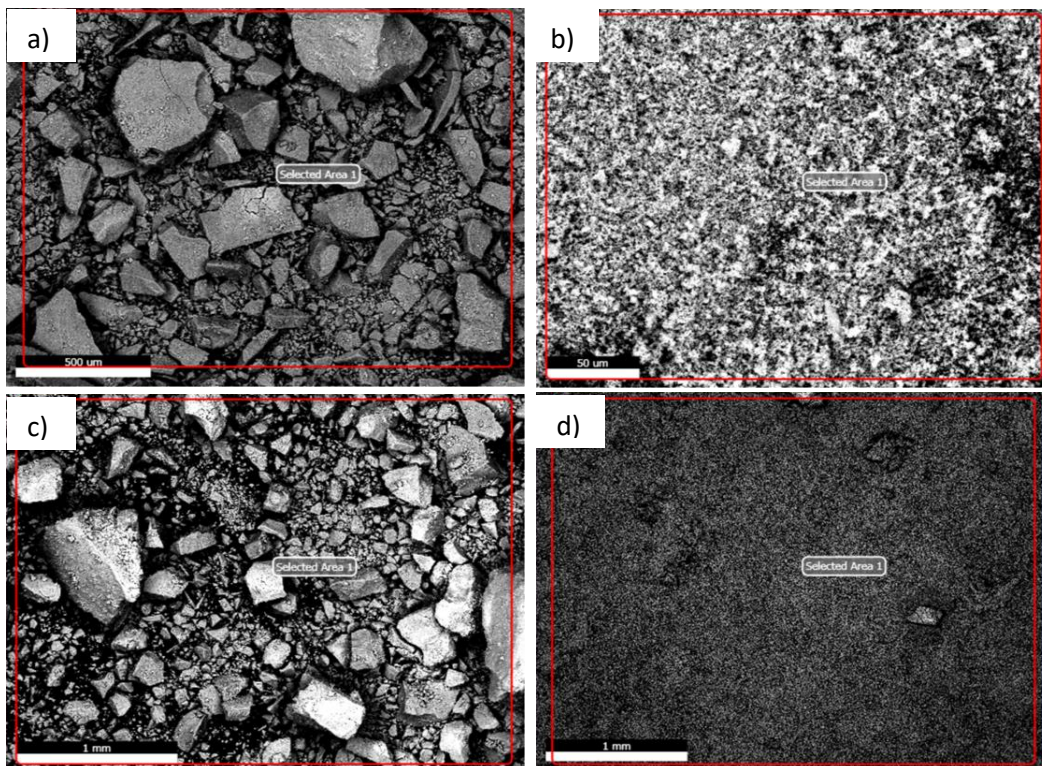
Image 7. a) Sample JA07 area 6, b) sample JA09 area 3, c) sample JA10 area 1, and d) sample JA11 (JA09 washed) area 3.

Sample name	Atomic (%)			
	Zr	S	C	O
JA07	7.85	1.80	37	53
JA09	4.95	0.86	41	52
JA10	3.58	0.95	50	45
JA09 (washed)	4.40	0.09	55	40

Table 9. Shows excerpts of atomic % of elements from eZAF Smart Quant Results.

The EDS measurement showed higher atomic percentage of zirconium as well as sulfur in JA07 than in JA10, see table 9. This could perhaps be explained by unreacted zirconium salt still present in the sample. Sample JA09 showed much higher traces of sulfur than expected. JA09 should not contain sulfur. Most likely the high traces of sulfur is due to residual sulfur ions from the zirconium sulphate salt that is still present in the MOF structure. A follow-up SEM-EDS analysis of JA09 was done after being washed. The figure can be found in section B.2 in the appendix. Descirption of washing procedure can be found in section B.1 JA09. Indeed, after washing only very small traces of sulfur remained. Comparing c) and d) in image 8 confirms that non-MOF chemical entities were washed out. What's more, the crystals of JA09 showed no sign of deteriation after washing.
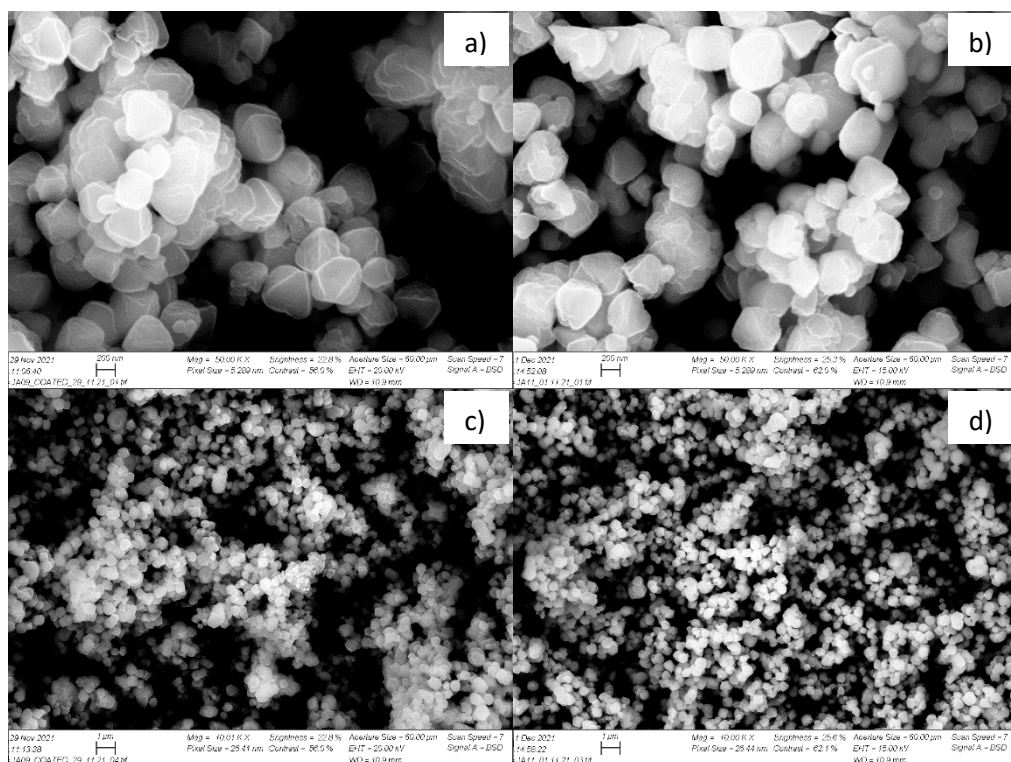
Image 8. Crystals of JA09 before and after washing.

Note: JA07 and JA10 were charging. Obtaining good images was not possible for these samples.

4.6.1 Contaminants
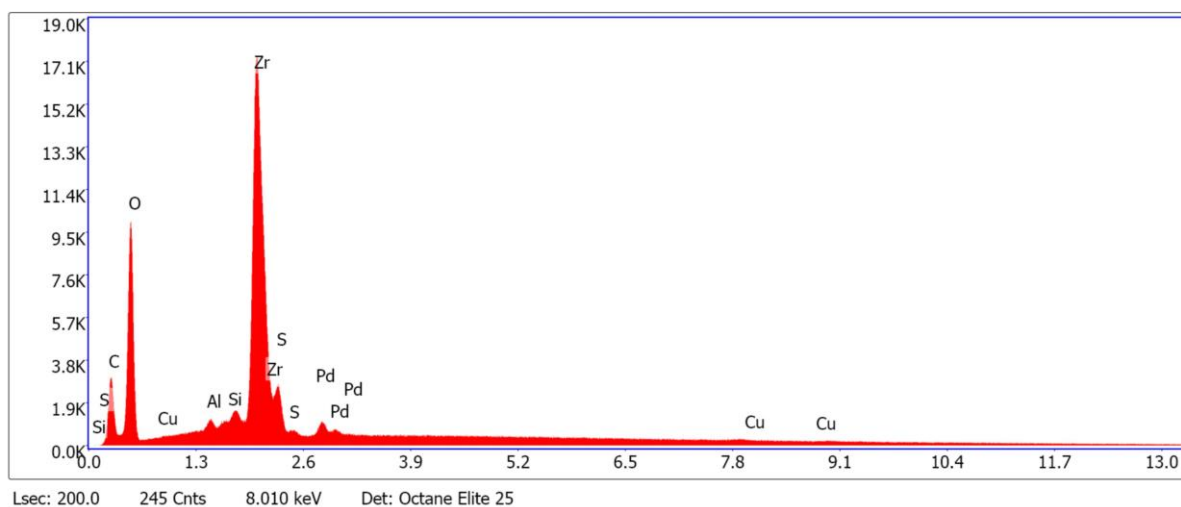
Figure 15. EDS graph of sample JA07 area 3.

EDS measurements of all three samples showed contaminants of copper (Cu), silisium (Si) and aluminium (Al). For graphs of JA09 and JA10 see appendix section B.2. Reagents used are not 100% pure. The tiny trace amounts of chemical units is likely from impurities in the chemicals used. Unfortunately, this can not be corroborated as the manufacturers do not give information regarding the chemical identities of possible impurities.

4.7 Batch adsorption results

Results before and after adsorption are given in tables 10, 11, and 12. Samples were used as synthesised in the adsorption experiments.

| Solution number	pH measurement	Conductivity measurement (μS/cm)
#1	7.18 (20.3 °C)	290 (20.3 °C)
#2	7.25 (20.3 °C)	462 (20.3 °C)
#3	7.18 (20.3 °C)	840 (20.3 °C)
#4	7.05 (20.3 °C)	1746 (20.3 °C)
#5	6.97 (20.3 °C)	3230 (20.3 °C)

Table 10. Results of stock solutions before adsorption in the metal uptake study.

Solution number	pH measurement	Conductivity measurement (μS/cm)
JA09-1	3.00	619
JA09-2	2.90	810
JA09-3	2.83	1368
JA09-4	2.80	2110
JA09-5	2.73	3720

Table 11. Results of JA09 solutions after adsorption in the metal uptake study.

Solution number	pH measurement	Conductivity measurement (μS/cm)
JA10-1	2.14	2420
JA10-2	2.13	2540
JA10-3	2.12	2930
JA10-4	2.12	3930
JA10-5	2.10	5420

Table 12. Results of JA10 solutions after adsorption in the metal uptake study.

The metal-chloride solutions that were measured before and after adsorption shows a trend in conductivity as well as for pH values. The expectation was that after adsorption the solutions would show an increase in acidity and a decrease in conductivity. Before adsorption the conductivity should be increasing with the number of ions in the solution, pH on the other hand is not expected to change significantly until after the adsorption experiment.
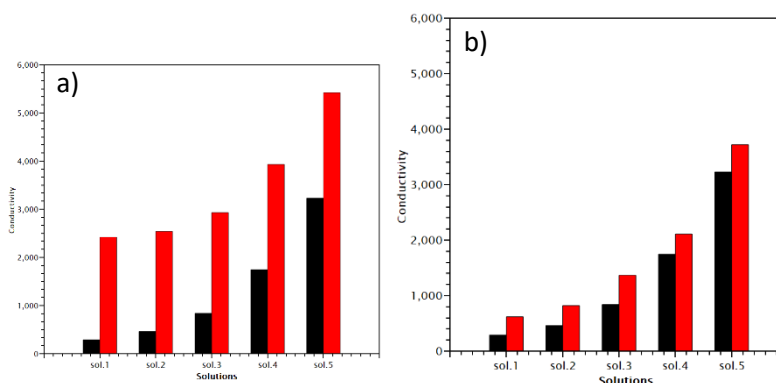
Figure 16. Conduvtivity meas., before (black) and after (red): a) JA10; b) JA09.

4.7.1 ICP-OES

Element:	Li added	Li measured		
Sample:	Stock sol.	Stock sol.	JA09	JA10
Sample nr.:		mg/L		
#1	14.4	22.3	13.8*	15.7
#2	28.7	30.5	29.2*	23.6
#3	57.4	60.7	58.1	47.6
#4	115	112	110	119
#5	230	225	225	225

Table 13. The samples for ICP-OES analysis were filtered through a 0.2 μm PVDF syringe filter before being received at the ICP laboratory (not the ref. samples). Samples and ref.samples were further diluted with 5% HNO3 prior to analysis. *The sample contained a small amount of turbidity/precipitate.
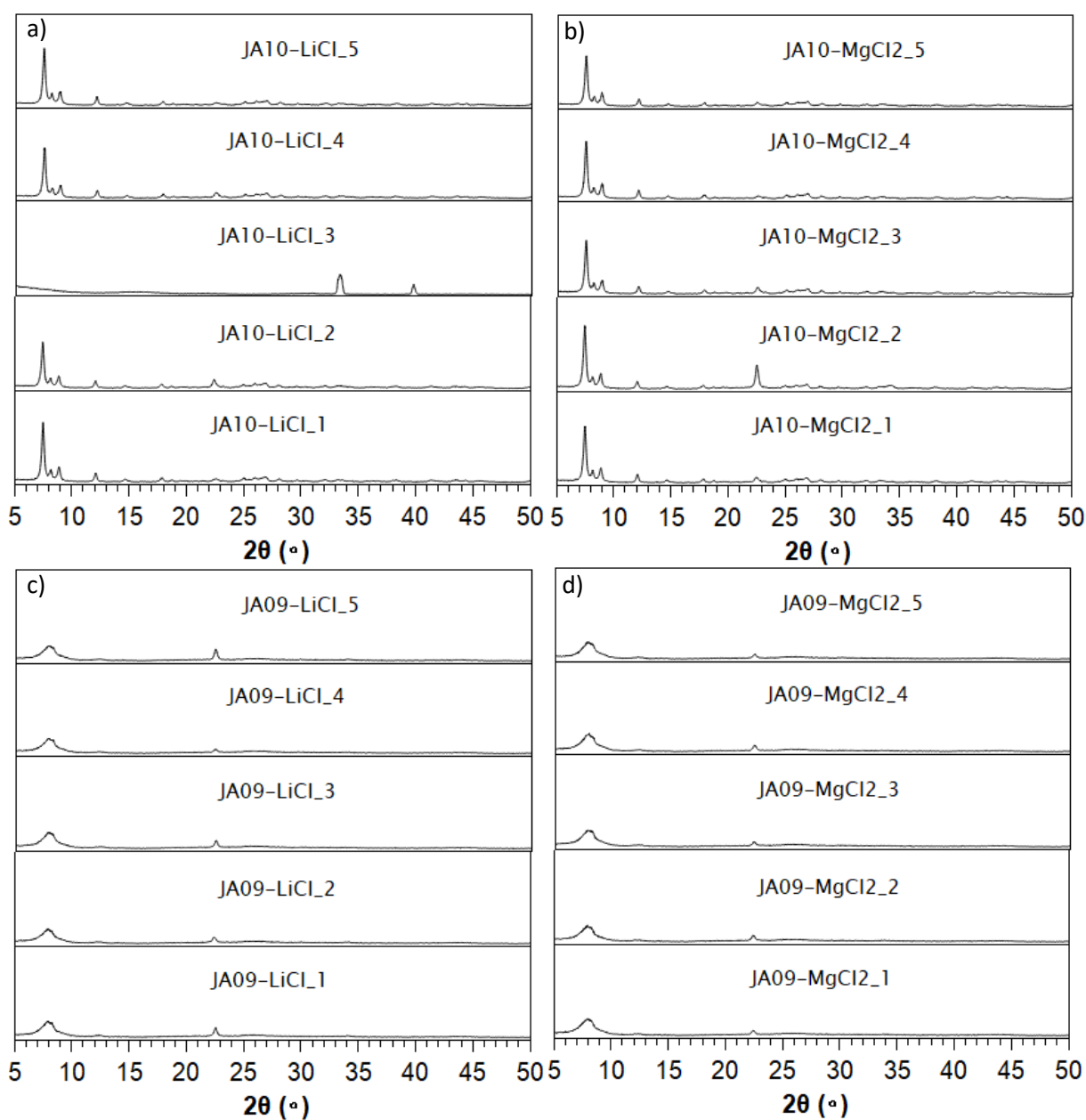
Figure 17. PXRD of MOF samples after metal uptake study: a) JA10 lithium uptake, b) JA10 magnesium uptake, c) JA09 lithium uptake, and d) JA09 magnesium uptake. Note: The inconsistency of JA10-3-Li must be due to human error.
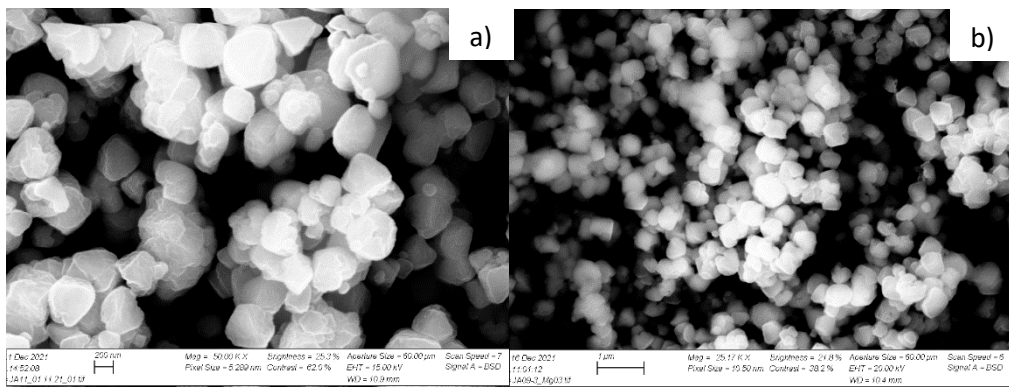
Image 9. SEM images: a) JA09-3-Mg; b) JA09 (after washing).
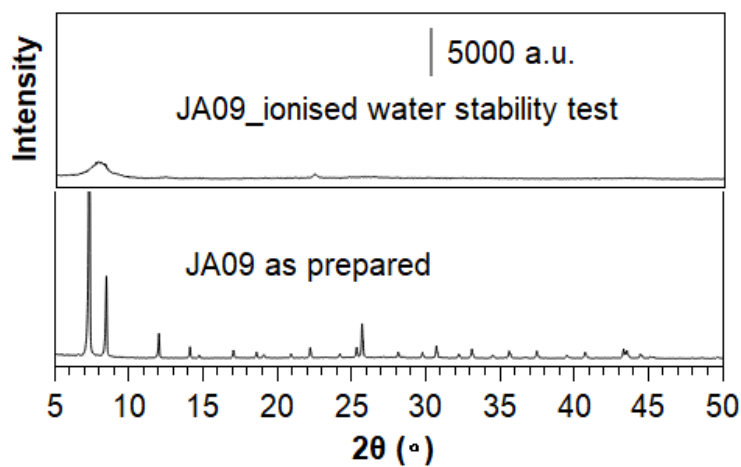
Figure 18. Sample JA09 (blank sample adsorption).

ICP-OES and SEM-EDS did not indicate successful adsorption of metal ions. PXRD results of the MOF samples after adsorption showed that while JA10 samples still had their structure intact – with the exception of JA10-Li-3. The JA09 samples on the other hand had lost their crystallinity judging from the PXRD findings. Unexpectedly, SEM images showed crystals from JA09-3-Mg to be in what looks like good shape, see image 9. EDS measurements showed tiny traces of magnesium in JA10 (0.02 – 0,18 atomic %). Although, a noticeable decrease in sulfur was also found (0.95 → 0.11) in the case of JA10-4-Mg. Sample JA09 was found not to be stable in a blank (ionised water only) solution, see figure 18.
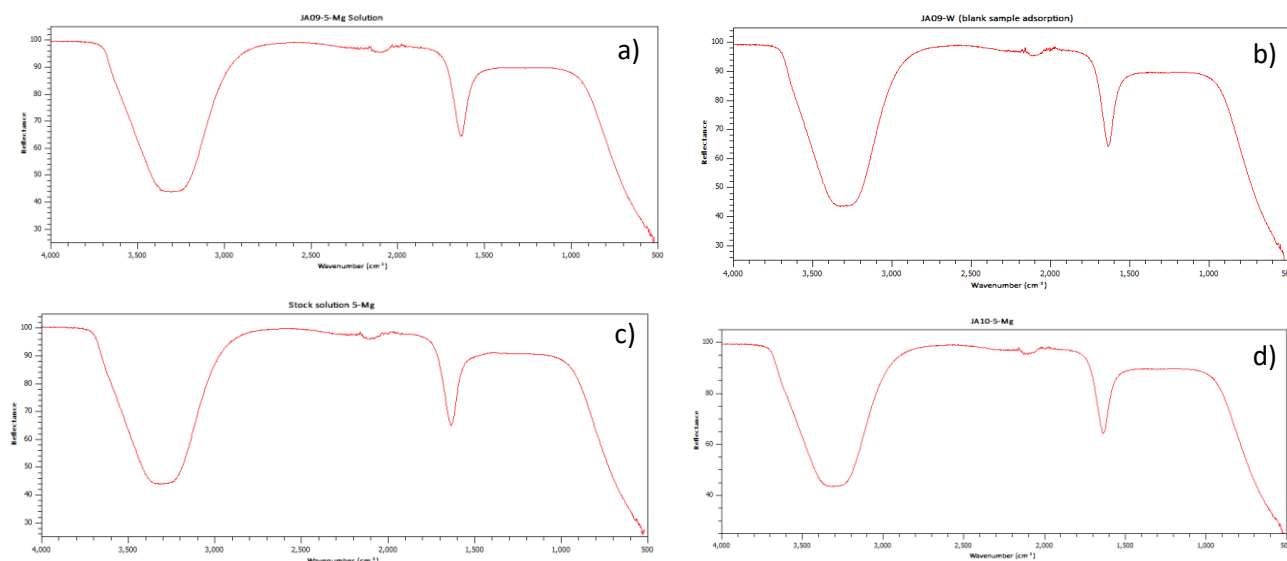
Figure 19. Solutions left after metal uptake study: a) JA09-5-Mg; b) JA09-W (blank sample adsorption); c) stock solution 5-Mg; d) JA10-5-Mg. MOFs were separated via centrifuge and then solution was extracted with syringe and 0.2 µm filters.

IR performed on one of each solution from the metal uptake study shows that there is no sign of residual MOF or linker left in the solution (figure 19). TGA of samples JA10-2-Mg and JA10-3-Li does not show any significant difference. No structural changes can be deducted from the TGA.
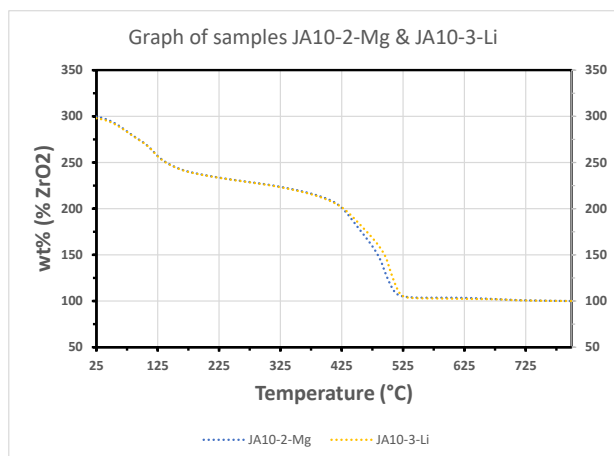
Figure 20. TGA of JA10-2-Mg and JA10-3-Li.

5. Conclusion

In this thesis zirconium-based MOFs UiO-66-BDC-COOH and Zr-BDC-(COOH)$_2$ were successfully synthesised and characterised. Both were employed in metal adsorption studies. The samples showing the strongest results were JA01 and JA04. Both showed ample crystallinity and thermal stability. Upscaled synthesis of JA01 and JA04 were carried out to make enough sample quantity for batch adsorption.

JA09 was found not to be chemically stable in water. While JA10 was stable in water, it did not show significant uptake of either lithium or magnesium. Sulfur content of JA10 did decrease after the batch adsorption. A trend could be found in measurements of pH and conductivity in the batch adsorption solutions. The pH value decreased significantly and the conductivity increased – particularly for JA10.

It is uncertain what has caused the drastic increase of acidity in the solutions after adsorption. IR analysis did not identify residual linker. While the increase in protons (H$^+$) can explain an increase in conductivity via proton jumping, also known as the Grotthuss mechanism [41], it's unlikely that proton jumping can be the sole explanation of the measured conductivity. Sulfur ions may have dissasociated from the samples as there will be residual unreacted sulfur in the MOF structure – from the synthesis with modulator especially. Solutions of JA10 shows significant increase in conductivity, also the JA09 sample had to be washed as there was found traces of sulfur, even after washing, still there were trace amounts of sulfur.

6. Future work

In this thesis work the batch adsorptions were carried out at room temperature and without modifying the pH of the solutions. Future work could do batch adsorption for different parameters. Increasing the basicity/temperature could yield better results and are worth trying.

JA05 and JA07 had a surprising twist when comparing the two. JA05 showed better crystallinity, but it was however not thermally stable. Somehow JA07 showed good thermal stability despite signs of poor crystallinity. This oddity could be examined closer by synthesising more samples and performing characterisations. If a stable synthesis of Zr-BDC-(COOH)$_2$ not employing sulfuric acid is possible it would mean even "greener" synthesis of Zr-MOFs.

Sources

[1] United Nations Treaty Collection. "7. d Paris Agreement." un.org. https://treaties.un.org/pages/ViewDetails.aspx?src=TREATY&mtdsg_no=XXVII-7-d&chapter=27&clang=_en (Downloaded: 28.12.2021)

[2] United Nations Climate Change. "Paris Agreement." unfccc.int. https://unfccc.int/sites/default/files/english_paris_agreement.pdf (Downloaded: 28.12.2021)

[3] Luis A. Gil-Alana, Manuel Monge, "Lithium: Production and estimated consumption. Evidence of persistence," *Resources Policy*, Volume 60, 2019, Pages 198-202, ISSN 0301-4207. https://doi.org/10.1016/j.resourpol.2019.01.006

[4] National Minerals Information Center. "Lithium (2016)." usgs.gov. https://www.usgs.gov/centers/national-minerals-information-center/lithium-statistics-and-information (Dated: 29. November 2016)

[5] Jiri Sterba, Alicja Krzemień, Pedro Riesgo Fernández, Carmen Escanciano García-Miranda, Gregorio Fidalgo Valverde, "Lithium mining: Accelerating the transition to sustainable energy", *Resources Policy*, Volume 62, 2019, Pages 416-426, ISSN 0301-4207. https://doi.org/10.1016/j.resourpol.2019.05.002

[6] U.S. Geological Survey. "Mineral Commodity Summaries 2021." usgs.gov. https://doi.org/10.3133/mcs2021 (Downloaded: 28.12.2021)

[7] Jasmina Hafizovic Cavka, Søren Jakobsen, Unni Olsbye, Nathalie Guillou, Carlo Lamberti, Silvia Bordiga, and Karl Petter Lillerud, "A New Zirconium Inorganic Building Brick Forming Metal Organic Frameworks with Exceptional Stability," *Journal of the American Chemical Society* 2008 *130* (42), 13850-13851. DOI: 10.1021/ja8057953

[8] Helge Reinsch et al., "Green synthesis of zirconium-MOFs†," *CrystEngComm*, 2015, 17, 4070-4074. DOI: https://doi.org/10.1039/C5CE00618J

[9] Sigma-Aldrich, "N,N-Dimethylformamide," SDS 227056, [Online]. Print date: 30.12.2021. Revision date: 16.07.2021. https://www.sigmaaldrich.com/NO/en/sds/sial/227056 (Downloaded: 28.12.2021)

[10] Q. Yang et al., "A Water Stable Metal–Organic Framework with Optimal Features for CO2 Capture†," *Angew. Chem. Int. Ed.*, 52: 10316-10320. https://doi.org/10.1002/anie.201302682

[11] Hanna Vikström, Simon Davidsson, Mikael Höök, "Lithium availability and future production outlooks," *Applied Energy*, Volume 110, 2013, Pages 252-266, ISSN 0306-2619. https://doi.org/10.1016/j.apenergy.2013.04.005

[12] T. J. Brown et al., "World Mineral Production 2015-2019," British Geological Survey, Nottingham, UK, 96pp. 2021. [Online]. http://nora.nerc.ac.uk/id/eprint/529923 (Downloaded: 28.12.2021)

[13] Neil G Connelly, Ture Damhus, Richard M Hartshorn, Alan T Hutton, "Nomenclature of Inorganic Chemistry: IUPAC Recommendations 2005," IUPAC, 2021. [Online]. https://iupac.org/wp-content/uploads/2016/07/Red_Book_2005.pdf (Downloaded: 28.12.2021)

[14] Omar M. Yaghi, Markus J. Kalmutzki, Christian S. Diercks, "Emergence of Metal-Organic Frameworks," *Introduction to Reticular Chemistry: Metal-Organic Frameworks and Covalent Organic Frameworks*, pp. 1-27, 29. March, 2019. [Online]. ISBN:9783527821099 DOI:10.1002/9783527821099

[15] S. R. Batten et al., "Coordination polymers, metal–organic frameworks and the need for terminology guidelines," *CrystEngComm*, 2012,14, 3001-3004. DOI: 10.1039/C2CE06488J

[16] Hira Saleem, Uzaira Rafique, Robert P. Davies, "Investigations on post-synthetically modified UiO-66-NH2 for the adsorptive removal of heavy metal ions from aqueous solution," *Microporous and Mesoporous Materials*, Volume 221, 2016, Pages 238-244, ISSN 1387-1811. https://doi.org/10.1016/j.micromeso.2015.09.043

[17] K. P. Lillerud et al., "A New Zirconium Inorganic Building Brick Forming Metal Organic Frameworks with Exceptional Stability," *J. Am. Chem. Soc.* 2008, 130, 42, 13850–13851. https://doi.org/10.1021/ja8057953

[18] Groom, C. R., Bruno, I. J., Lightfoot, M. P. & Ward, S. C., "The Cambridge Structural Database," *Acta Cryst*. 2016, B72, 171-179. https://doi.org/10.1107/S2052520616003954

[19] Seungkyu Lee, Hans-Beat Bürgi, Sultan A. Alshmimri, and Omar M. Yaghi, "Impact of Disordered Guest–Framework Interactions on the Crystallography of Metal–Organic Frameworks," *J. Am. Chem. Soc.* 2018, 140, 28, 8958–8964. https://doi.org/10.1021/jacs.8b05271

[20] Susan E. Bailey, Trudy J. Olin, R.Mark Bricka, D.Dean Adrian, "A review of potentially low-cost sorbents for heavy metals", *Water Research*, Volume 33, Issue 11, 1999, Pages 2469-2479, ISSN 0043-1354. https://doi.org/10.1016/S0043-1354(98)00475-8

[21] Q. Qian et al., "MOF-Based Membranes for Gas Separations," *Chem. Rev*. 2020, 120, 16, 8161–8266. https://doi.org/10.1021/acs.chemrev.0c00119

[22] Hao Li, Kecheng Wang, Yujia Sun, Christina T. Lollar, Jialuo Li, Hong-Cai Zhou, "Recent advances in gas storage and separation using metal–organic frameworks," *Materials Today*, Volume 21, Issue 2, 2018, Pages 108-121, ISSN 1369-7021. https://doi.org/10.1016/j.mattod.2017.07.006

[23] Shekhah, O., Chernikova, V., Belmabkhout, Y., Eddaoudi, M., "Metal–Organic Framework Membranes: From Fabrication to Gas Separation," *Crystals* 2018, 8(11), 412. https://doi.org/10.3390/cryst8110412

[24] D. T. Sun et al., "Rapid, Selective Heavy Metal Removal from Water by a Metal–Organic Framework/Polydopamine Composite," *ACS Cent. Sci*. 2018, 4, 3, 349–356. https://doi.org/10.1021/acscentsci.7b00605

[25] Peng, Yaguang & Huang, Hongliang & Zhang, Yuxi & Kang, Chufan & Chen, Shuangming & Song, Li & Liu, Dahuan & Zhong, Chongli. "A versatile MOF-based trap for heavy metal ion capture and dispersion," *Nature Communications* (2018). 9. 10.1038/s41467-017-02600-2. DOI: 10.1038/s41467-017-02600-2

[26] Johnson E. Efome, Dipak Rana, Takeshi Matsuura and Christopher Q. Lan, "Metal–organic frameworks supported on nanofibers to remove heavy metals†," *J. Mater. Chem. A*, 2018, 6, 4550-4555. https://doi.org/10.1039/C7TA10428F

[27] Fátima Arroyo, José Morillo, José Usero, Daniel Rosado, Hicham El Bakouri, "Lithium recovery from desalination brines using specific ion-exchange resins," *Desalination*, Volume 468, 2019, 114073, ISSN 0011-9164, https://doi.org/10.1016/j.desal.2019.114073

[28] Sung Ho Park, Kiwoong Kim, Jae Hong Lim, Sang Joon Lee, "Selective lithium and magnesium adsorption by phosphonate metal-organic framework-incorporated alginate hydrogel inspired from

lithium adsorption characteristics of brown algae," *Separation and Purification Technology*, Volume 212, 2019, Pages 611-618, ISSN 1383-5866. https://doi.org/10.1016/j.seppur.2018.11.067

[29] Emilia Olsson, Guoliang Chai, Martin Dove, Qiong Cai, "Adsorption and migration of alkali metals (Li, Na, and K) on pristine and defective graphene surfaces†," *Nanoscale*, 2019,11, 5274-5284. https://doi.org/10.1039/C8NR10383F

[30] Renu, Madhu Agarwal, K. Singh, "Heavy metal removal from wastewater using various adsorbents: a review," *Journal of Water Reuse and Desalination*, 1. December, 2017, 7 (4): 387–419. doi: https://doi.org/10.2166/wrd.2016.104

[31] H. Reinsch et al., "PROCESS FOR PREPARING A ZIRCONIUM-BASED METAL ORGANIC FRAMEWORK," US 10,450,330 B2, 22.10.2019. [Online]. https://patents.google.com/patent/EP3197902A1/en

[32] Geoff Rayner-Canham, Tina Overton. (2014). *Descriptive Inorganic Chemistry: Sixth Edition*. ISBN: 978-1-319-15411-0. W. H. Freeman and Company, 41 Madison Avenue, New York, NY 10010.

[33] H. Wu et al., "Unusual and Highly Tunable Missing-Linker Defects in Zirconium Metal–Organic Framework UiO-66 and Their Important Effects on Gas Adsorption," *J. Am. Chem. Soc*. 2013, 135, 28, 10525–10532. https://doi.org/10.1021/ja404514r

[34] S. Yuan et al., "Stable Metal-Organic Frameworks: Design, Synthesis, and Applications," *Adv Mater*. 2018, 30, 1704303. https://doi.org/10.1002/adma.201704303

[35] National Center for Biotechnology Information. "PubChem Compound Summary for CID 10708, 1,2,4-Benzenetricarboxylic acid," *PubChem*, https://pubchem.ncbi.nlm.nih.gov/compound/1_2_4-Benzenetricarboxylic-acid (Accessed 30. December 2021)

[36] National Center for Biotechnology Information. "PubChem Compound Summary for CID 6961, Pyromellitic acid," *PubChem*, https://pubchem.ncbi.nlm.nih.gov/compound/Pyromellitic-acid (Accessed 30. December 2021)

[37] Wikipedia. "Brine mining." Wikipedia.org. https://en.wikipedia.org/wiki/Brine_mining (Accessed 30. December 2021)

[38] Andrei A. Bunaciu, Elena gabriela Udriştioiu & Hassan Y. Aboul-Enein, "X-Ray Diffraction: Instrumentation and Applications," *Critical Reviews in Analytical Chemistry,* 2015, 45:4, 289-299. https://doi.org/10.1080/10408347.2014.949616

[39] J. G. M. van Berkum, R. Delhez, Th. H. de Keijser and E. J. Mittemeijer, "Diffraction-Line Broadening due to Strain Fields in Materials; Fundamental Aspects and Methods of Analysis," *Acta Cryst*. (1996). A52, 730-747. https://doi.org/10.1107/S0108767396005727

[40] Sigma-Aldrich. "1,2,4-Benzenetricarboxylic acid." sigmaaldrich.com. https://www.sigmaaldrich.com/NO/en/product/aldrich/b4589 (Accessed 30.12.2021)

[41] Wikipedia. "Grotthuss mechanism." Wikipedia.org. https://en.wikipedia.org/wiki/Grotthuss_mechanism (Accessed 31. December 2021)

7. Appendix

A. Theory section

A.1 Unit cells

To help explain the theories of this thesis it is productive to first consider unit cells as its concept will make it easier to visualise metal-organic structures (MOFs) and powder x-ray diffraction (PXRD) in particular.

A.1.1 Crystal structure

In a crystalline material the atoms, molecules or ions are naturally arranged into an ordered structure. Conceptually a crystal is a composite of basic building blocks called unit cells (figure S1) that repeat by translations in three-dimensional space creating a crystal lattice. The lengths of the edges in the unit cell are a,b,c and its angles between said angles are α,β,γ. Every atom inside the crystal is covered by crystal planes and are visualized and identified via Miller notation (h,k,l). These Miller indices are used to define a unique set of planes in the crystal which can then be used as a subscript. For example, d_{hkl} refers to the distance between the planes defined by hkl [1].

For the purpose of this thesis unit cells of cubic shape will be focused on. There are three varieties of cubic crystals, they are simple cubic (cP), body-centred cubic (bcc) and face-centred cubic (fcc), see figure S1 [2].
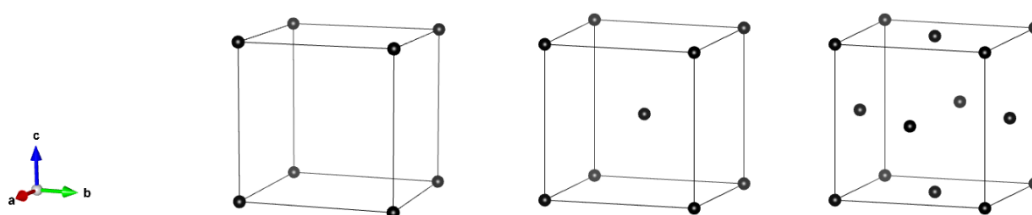
Figure S1: From left to right simple cubic lattice structure, body-centred cubic structure, and face-centred cubic structure.

Figure S1 demonstrates the cubic structures. In the simple cubic system, the unit cell has lattice points in each corner of the cube. Lattice points are points in space where particles are free to vibrate [3]. Like previously mentioned the convention is that unit cells repeat, which means there are neighbouring unit cells that also have lattice points in their corners, and whose particles are identical. These lattice cells are shared between the unit cells [2].

The simplest repeating unit cell in a simple cubic structure is the simple cubic cell, see left on figure S1. It could contain other particles, but for a material to be classified as having a simple cubic structure it *must* have eight identical particles at the same lattice points of the unit cell. The body-centred cubic system expands on the simple cubic structure, which means it has, along with the eight identical particles in each corner, an additional lattice point in the unit cell centre, see middle on figure 1. The face-centred cubic system expands on the simple cubic structure in a different way. On the face-centred cube there are additional lattice points on the four faces of the unit cell [3].

Seeing as the eight corner particles are shared between unit cells repeating in each direction, these points are therefore shared by eight unit cells. Since each lattice point in a simple cubic structure is occupied by an atom, then through sharing with eight other unit cells in each lattice point the unit cell will contain one atom, specifically ($\frac{1}{8} \times 8$). Analogously a body-centred cubic structure willcontain two

atoms, specifically $1 + (\frac{1}{8} \times 8)$, that is one atom in the middle and one atom from sharing lattice points in each corner. Furthermore, a face-centred cubic structure will contain four atoms, specifically $(\frac{1}{8} \times 8) + (\frac{1}{2} \times 6)$, where in addition to the shared corner lattice points, each of the six faces of the unit cells share half its lattice point [3].

A.1.2 Ligancy

Coordination number tells how many neighbours of a central atom there are. These neighbours may be referred to as ligands, and the coordination number may also be called ligancy. For crystal structures the way ligancy is found is by using the unit cell as a model. It is the shared lattice points that are counted as being ligands. This means that the simple cubic unit cell structure has eight ligands, same case for bcc. Face-centred structure unit cells on the other hand has fourteen ligands because it also shares in each of the six cube faces [4].

A.2 MOF defects

The unit cells show ideal MOF structure, meanwhile in the real material there are defects, which means not every metal-cluster will have as many coordinated organic linkers as in the ideal unit cell case. The porosity of the MOFs is hurt by defects, but they can be managed by changing the conditions of the synthesis.

A.2.1 Missing linker

Defects compromise the MOF structure in different ways. Reduced connectivity in the framework would weaken the structural stability [5]. Missing linker defects means the MOF structure will contain other ligands to balance the charge of the metal cluster [6].

The defect ligands are expected to compromise the chemical, physical and thermal stability of the structure, due to less connectivity. The identity of the ligands will impact the porosity of the and surface area of the MOF structure. Where smaller units will cause larger empty spaces inside the structure, while larger units will cause greater surface area. These features could prove to be desirable granted it can operate with defects without decomposing [6].

A.2.2 Missing cluster defects

Like in the case of missing linker defects, missing cluster defects is expected to alter the MOF structure. When the structure forms missing clusters, it means the neighbouring SBUs will have a vacant spot, and its vacancy must be compensated by water, hydroxide, or other species [6]. The missing clusters become compensated for by other ligands, which effectively compromises the thermal stability, although they also yield greater surface area [6]. Just like with linker defects, the defects of metal clusters correspond to less connectivity in the framework, thus similarly larger empty pores are to be expected.

A.2.3 Modulator

A modulator can be added to the reaction mixture during the synthesis to modulate the MOF structure. That is the equilibrium of the crystallisation process becomes partially obstructed, and therewith slow down. Obstruction comes about from modulator molecules coordinating to the zirconium ions which blocks direct interaction between the node and the linker. This means the linker molecules must go through the process of substituting the modulator molecules, which is what slows down the reaction rate [6][7].

The addition of modulator is expected to result in products of higher crystallinity. However, it is possible that the product still contains zirconium ions with coordinated modulator molecules not yet substituted, and consequently the structure will have defects. What's more, this opens up another avenue for tuning the MOF structure. By employing different concentrations of modulator, it is possible to tune number of defects, pore volume, particle size, morphology, and product crystallinity [6].

A.3 Description of powder x-ray diffraction

Powder x-ray diffraction (PXRD) is an easy, straightforward, and non-destructive way to analyse powder samples. Sample preparation requires only a few minutes. The scanning itself only requires 15 – 20 minutes. Not much sample powder is needed. Although PXRD also does have some limitations. Sample identification works best when the powder is fine and homogeneous. For the interpretation of data collected it must be compared to a reference, that is access to reference data is required. Finally, peak overlay can happen, and reflections are magnified if angles are high [8].

Powder x-ray diffraction is a tool for characterising and analysing crystalline materials without destroying said material. Electromagnetic waves are beamed at a sample and is diffracted by the atoms in the sample. Diffraction comes about when electromagnetic radiation interacts with a periodic structure like crystalline materials. The beam of electromagnetic radiation will at certain wavelengths and at certain angles reflect the radiation. These reflected beams can add together and reinforce each other. Intensity of the reflection-peaks are dictated by the atoms and their position in the crystal lattice [8].

Electromagnetic radiation behaves like a wave. Interference describes how two waves interact with each other. There are two types of interference, constructive and destructive. Constructive interference means the wave's peaks are in phase, while destructive interference means that the peaks are out phase, see figure 5. Perfect destructive interference means the peaks are 180° out of phase [9]. The intensity of reflection can thusly be explained by constructive interference. That means the waves being scattered by the atoms in the crystal lattice are moving in phase with each other.
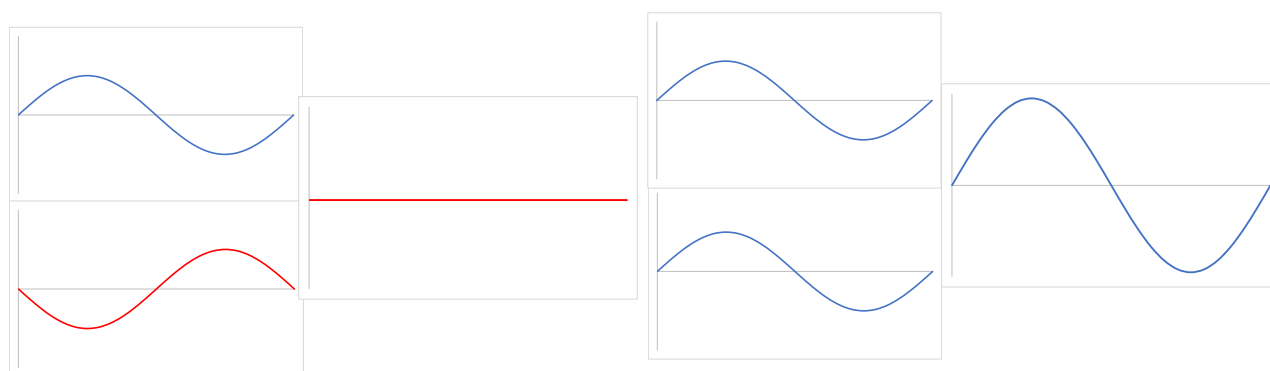

Figure S2. Visual representation of concept of inference phenomena of waves.

A model describes how the radiation diffracts when it interacts with the crystalline surface, and is called Bragg's law:

$$2dsin\theta = n\lambda$$

(1)

In the model *d* represents a constant distance between each plane in the lattice – also called interplanar spacing. Theta, ϑ, represents the angle of diffraction, while *n* is an integer, and lambda, λ, is the wavelength of the x-rays [8]. Bragg's law tells the relationship between the lattice spacing together with the diffraction angle, and the wavelength of electromagnetic radiation.
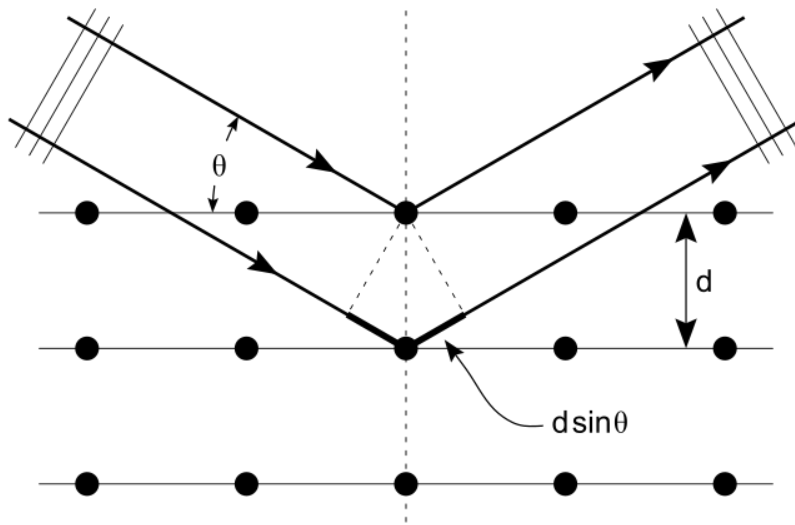

Figure S3. Bragg diffraction [10].

By picking up the reflected beams from constructive diffraction, along with employment of Bragg's law, a diffraction pattern can be plotted. These patterns can be thought of as "fingerprints". This means the patterns can be compared to analyse whether the crystalline material has any similarity with other crystalline materials, or it can be compared to calculated patterns to see if the material has any matching peaks.

A.3.1 Instrument operation

The sample is placed on a track with slots suited for flat sample holders. A cathode ray tube generates x-rays that are accelerated at the sample. The sample rotates while in aim of the x-ray beam at an angle, θ, meanwhile an x-ray detector that is mounted on an arm collects diffracted x-rays while rotating at angle, 2θ. The x-rays when making impact on the sample will at certain angles satisfy Bragg's law and constructive interference comes about, creating a peak in intensity. This reflected signal x-ray is recorded by the detector in the instrument. The signal is converted to a count rate, and then output from the recorder to a computer. Data collection for typical powder patterns are collected at 2θ from 5° to 70°. The instrument scans the material over a range of 2θ angles because the sample in powder x-ray diffraction is *powder*. This means scanning over a range of angles will give all possible diffraction angles thanks to the crystals' random orientation [8].

As previously mentioned, the occurrence of constructive interference is related to the material's structure, more specifically from the interplanar spacing between layers in the lattice. When the repeating distance of the periodic structure and the radiation wavelength are around the same magnitude diffraction will occur. This is why x-rays are used as their wavelengths have the appropriate magnitude. The diffraction peaks will correlate to the compounds unique d-spacings. By converting diffraction peaks to d-spacings, the pattern that emerges can be compared to reference patterns from literature or calculation.

A.4 Thermogravimetric analysis TGA

A.4.1 Description of thermogravimetric analysis

Thermogravimetric analysis (TGA) is a method of examining a sample by applying heat to it and measuring its mass during the rise in temperature. The measurement is performed in a closed and controlled atmosphere. Mass loss come about due to chemical or physical processes following the heat increase, and if applicable – depending on the simulated atmosphere – reactions with the atmosphere [11][12].

TG analysis can be performed in different ways. The different procedures are called dynamic, static, and quasistatic. Dynamic TGA means the temperature continuously increase over time while mass is recorded. Such procedures give the amount of gas removed with the temperature of when it occurs simultaneously. For static TGA, instead of increasing the temperature it's held constant while measuring the sample mass. This is useful for gathering information for a certain temperature point, like whether the sample is able to withstand that temperature point, or how exactly does the sample decompose at the given temperature. Finally, quasistatic TGA heats the sample in various temperature intervals, but also holds the temperature constant at these intervals over a duration. This way a sample that is known to decompose in different ways at different temperatures can more precisely be looked at, giving better precision in its characterisation [12].

TGA plots can show where weight loss is most evident. Different curve shapes indicate different processes. A flat curve means there is no change in weight, and no mass loss. A steep decline at the beginning of the measurement means there is a desorption or drying process taking place in the material. Following mass loss may come as a single steep decline or as multiple, which is a multistage decomposition. A slow decline on the other hand can be due to no intermediates or the heating rate may be too fast. An increase of mass can be observed due to reaction with the atmosphere. It could for instance mean the sample has had an oxidation process on its surface. This mass increase may be lost at higher temperatures which would appear as a bump in the curve [12].

Weight loss is then due to chemical bonds being broken, causing decomposition, or loss of solvent and other volatile elements, that is evaporation or desorption, additionally, the atmosphere can react with the sample and cause a reduction. On the other side weight gain can also happen and is caused by sorption or oxidation from reacting with the atmosphere [12].

A.4.2 Weight change balance

When a change in mass occurs, there is an imbalance on the balancer that the sample sits on tips. There are light sensors on each side of the balancer receiving the same amount of light when the balance is at null (zero). The balancer is rectified by a current so that the light sensors get equal amounts of light, this current is tied to the shift in weight. Thusly can the instrument record change in sample weight [12].

A.4.3 Differential Scanning Calorimetry

The differential scanning calorimetry (DSC) technique for TGA, measures the difference in heat flow rate between the sample and an empty sample sensor for reference. The furnace has two spots to put the sample holder. The sample holder used in TGA is called a crucible. The difference in temperature between the two sample sensors is attributed to a change in the material of the non-empty sample sensor [12].

A.5 Adsorption theory

The adsorption process is a surface phenomenon where adsorptive entities like molecules, atoms or ions in a gas or liquid fluid are concentrated, by adhesion, on to the surface of a solid or at a fluid interface. In the adsorption process the adsorptive entities that are concentrating on to a solid surface or fluid interface are called adsorbate. While the solid surface or fluid interface is called adsorbent [13].
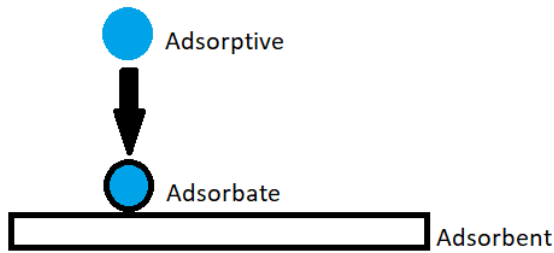

Figure S4. The top blue ball represents the adsorptive entities that are free flowing in the bulk fluid. The blue ball is then adsorbed onto a solid surface, which is here represented by a square.

There are different types of adsorption. Physical adsorption is caused by weak interactions between the adsorbent and the adsorptive, such as van der Waals and London dispersion forces. Chemical adsorption is caused by chemical bonding, such as ionic, covalent and hydrogen bonds. The inverse of this process is called desorption, that is the concentration of molecules, atom or ions is decreasing [14][15].

Adsorbents can be used to isolate a material, the adsorbate, from a solvent. Due to pores in the adsorbent material, it contains high surface area per unit volume [13]. When considering porous adsorbents there is a distinction between the external surface and the internal surface, and there are classifications of pore sizes [16]:

(i)   Pores of widths greater than 50 nm are called macropores.
(ii)   Pores of widths greater than 2 nm, but smaller than 50 nm are called mesopores.
(iii)   Pores of widths smaller than 2 nm are called micropores.
(iv)   Nanopores are all pores smaller than 100 nm.

When utilizing the adsorption phenomena for separation of an adsorbate there are several stages of operation that must be followed. First step is the adsorption itself. The adsorbate can be transferred from the bulk liquid in the solvent to the adsorbents, and then by diffusion the adsorbate can enter a pore and be transferred into the adsorbent. Next the adsorbate becomes adsorbed onto the larger inner surface area and has thus been isolated from the solvent. After the adsorption step is washing. The washing step is done to remove material that has not been adsorbed. Thereafter is desorption in a suitable solvent. This step is to get back the adsorbate from the adsorbent. Following this step too is washing, that is to rid the adsorbent of remaining material in its pores, hence the adsorbent is regenerated [13].

A.5.1 Adsorption isotherms

An adsorption isotherm describes the relationship between the adsorbate in the fluid and the adsorbate that is adsorbed on the surface of the adsorbent at a constant temperature [webinar]. For an adsorbate an isotherm can be found where the concentration of the adsorbate that is adsorbed is plotted versus the concentration that is unadsorbed. In order to describe the adsorption isotherm

there have been developed several models, but not one is without prerequisites. Adsorption equilibrium data must be determined experimentally [13]. The models that will be of most interest for this thesis is the Langmuir isotherm and the Freundlich isotherm.

A.5.1.1 Langmuir isotherm

The following equation is an expression for the Langmuir isotherm [9]:

$$C_{AS}^* = \frac{C_{ASm} \times K_A \times C_A^*}{1 + K_A \times C_A^*}$$

(2)

This Langmuir isotherm equation gives, C_{AS}^*, the equilibrium concentration or loading of adsorbate on the adsorbent. C_{ASm} represents the maximum loading of adsorbate corresponding to complete monolayer coverage of all available adsorption sites. C_A^* is the equilibrium concentration of solute in the fluid phase. K_A is a constant associated with the equilibrium.

Prerequisites of Langmuir adsorption [13]:

(i)   Adsorbed molecules form only one layer on the surface, called the monolayer.
(ii)   Each adsorption site is equivalent in terms of adsorption energy.
(iii)   No interactions between adjacent adsorbed molecules take place.
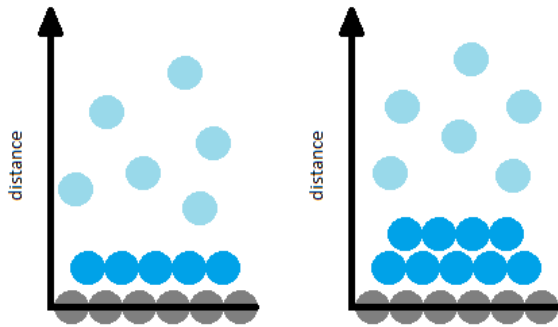
Figure S5. A conceptual representation of monolayer (left) and multilayer (right), in relation to adsorptive in the bulk fluid. Black balls represent adsorbent, blue balls are adsorbed molecules, and light blue balls are the adsorbate molecules in free flow.

Monolayer does not reflect the reality. We use the adsorption data to determine the statistical amount adsorbed, and for the Langmuir model adsorption is assumed to consist only of one layer – the monolayer, even though this does not reflect the reality [19][17]. The Langmuir adsorption model cannot accurately describe MOFs because its assumptions are that the adsorbate is chemisorbed in a single layer [17].

A.5.1.2 Freundlich isotherm

The following equation is an expression for the Freundlich isotherm [13]:

$$C_{AS}^* = K_F C_A^{*1/n}$$

(3)

This equation for the Freundlich isotherm gives, C^*_{AS}, the equilibrium concentration or loading of adsorbate on the adsorbent. The equilibrium concentration of solute in the fluid phase is represented again by C^*_{AS}. Lastly there are the constants K_F and n.

A.6 N₂-sorption

To determine the characteristics of porous solids and fine powder different techniques are employed. They are gas adsorption, air permeability and laser diffraction [19]. In this thesis, for determining the surface area and pore size of MOFs, gas adsorption was the chosen method.

In this method pure gas is given entry to a volume containing the adsorbent. The temperature is maintained at a constant value, also the volume containing adsorbent, and the amount of pure gas given entry to it are known [16]. Molecules from the gas phase is adsorbed to the sample's inner and outer surface, during which the pressure falls. At equilibrium the rate of adsorption and the rate of desorption will be equal, and pressure will no longer drop [16]. At this equilibrium pressure the amount of gas that has been adsorbed is explained as the amount gas that was given entry subtracted by the amount of gas that was needed to fill the space around the adsorbent [16].

A nitrogen adsorption measurement gives the adsorption isotherm for adsorbing nitrogen. The amount of gas adsorbed is determined and plotted versus equilibrium pressure, which – depending on the gas – is often expressed as relative pressure [webinar]. At high temperatures, like room temperature, the kinetic energy is so high that the molecules or ions are "trapped" for an intangible time frame. To be able to measure sorption then, the measurement is carried out at cryogenic temperatures – also temperature must be held constant, and the system needs adequate time to equilibrate [19][16].

To analyse the nitrogen adsorption isotherm, it is typical to use the Brunauer-Emmett-Teller (BET) model [16]. The BET model is employed to assess the pore size and surface area of the material. By applying BET theory one can use the nitrogen isotherm measurement to estimate the nitrogen monolayer loading, and in turn this estimation can be used to find the BET area [18].

A.6.1 BET Model for assessing the surface area

The BET method is mathematical model for analysing adsorption isotherms in order to find the monolayer capacity so an estimate for surface area can be determined [17]. Due to micropores' non-clear physical meaning, the concept of monolayer content in the BET model is not precisely representing the real monolayer capacity [17]. Also because of the unknown adsorbate packing microporous volume is not precise either [17].

A.6.1.1 Choice of adsorptive

The choice of nitrogen as the adsorptive has been standard by general consensus for analysis of adsorption of mesopore and micropore sizes. This choice of adsorptive however is not without flaws. The orientation of nitrogen molecules depends on the adsorbent's surface chemistry, this is because of nitrogen's quadrupole moment. Additionally, it affects the pressure of micropore filling. Other problems are the slow initial diffusion rate for MOFs at low pressure ranges, nitrogen molecules before they've been adsorbed can create blockades in micropores, pore filling pressure is not accurate due to specific interactions with surface functional groups, and lastly cryogenic temperatures create kinetic restrictions [16].

A.6.2 BET plots

Linear form [18]:

$$\frac{p}{V_A(p - p_0)} = \frac{1}{V_M \times C} + \frac{C - 1}{V_M \times C}\left(\frac{p}{p_0}\right)$$

(4)

Alternatively:

$$\frac{p}{n(p_0 - p)} = \frac{1}{n_m \times C} + \frac{C - 1}{n_m \times C}\left(\frac{p}{p_0}\right)$$

(5)

The equation shows the relationship between the adsorbed volume, V_A, and the relative pressure p/p_0, where p is the pressure and p_0 is the saturation pressure. The alternative equation similarly shows the relationship between the specific adsorbate amount, *n*, and the relative pressure p/p_0. *C*, V_M and n_m are empirical constants. *C* represents the adsorption energetics, while V_M and n_m represents the specific adsorbate monolayer volume and capacity respectively, and they are connected to the specific surface area of the material [18][16]. Note that equation 5 follows the linear equation expression. Thus, by linear regression the *C* and n_m values can be determined using equations 6 and 7.

$$n_m = \frac{1}{slope + intercept}$$

(6)

$$C = 1 + \frac{slope}{intercept}$$

(7)

The alternative equation uses micropore capacity, n_m, instead of the micropore volume, V_M, because the calculation of micropore volume depend on the adsorbate packing in the micropores [17].

Assumptions of the BET theory [17]:

(i)   Adsorption takes place on a uniform surface and the energies of adsorption of all molecules in the first layer are identical.
(ii)   Each molecule adsorbed in a layer is itself a potential adsorption site for the next layer.
(iii)   It is only for the first layer that the differential energy of physical adsorption E_1 is higher than the energy of liquefaction E_l.
(iv)   Interactions between molecules adsorbed in the same layer do not play any part in the adsorption equation.

Consistency criteria of BET theory [18][17][16]:

(i)   Only select a range that is entirely increasing, that is $n(p_0 – p)$ continually increases as p/p_0 increases.

(ii)   The value of C must be positive for the linear BET fit, a negative value would be impossible in the real world and therefore meaningless.

(iii)   When giving the adsorption isotherm, the monolayer loading, n_m and V_M, should correspond to a relative pressure, p/p_0, that is within the pressure range selected for the linear region used in the isotherm.

(iv)   The relative pressure corresponding to the monolayer loading calculated from BET theory should be equal to the pressure determined in criterion (iii).

In case a linear region satisfying all criteria cannot be found, then the linear region least deviating from the criteria is selected [18]. BET fit must be linear; C > 0. To satisfy BET consistency criteria the value R^2 > 0.995 is chosen, or whichever is highest. When plotting V_A/V_M vs. p/p_0 – where there is a "knee bend", we find the statistically established monolayer [19]. Should the material consist purely of micropores, it would be an ideal Type I isotherm, and the "knee bend" would then show the exact micropore capacity [17].

A.7 Scanning Electron Microscopy/Energy Dispersive X-ray Spectrometry (SEM-EDS)

A.7.1 Scanning Electron Microscopy (SEM)

A scanning electron microscope is an instrument that is used to study a sample's chemical composition, crystallography, and its shape and size [20]. Using an electron microscope allows for analysing samples at even smaller scales than light microscopes. This is thanks to the use of electrons over light as electrons have shorter wavelengths than visible light. Electron microscopes allow for significantly higher magnification compared to light microscopes. Additionally, SEM allow for greater depth of field.
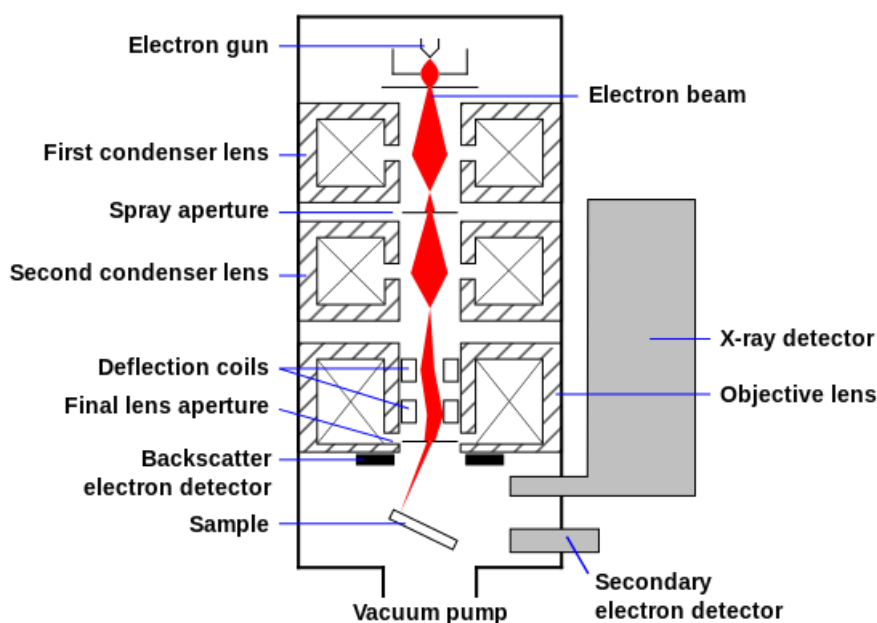
Figure S6. Schematic drawing of electron beam being modified before reaching the sample [21].

The way the instrument operates is by emitting an electron beam from an electron gun. The beam is passed through and modified by one or two condenser lenses, which may also be referred to as apertures, to narrow its diameter [20]. The beam continues passing through a pair of electromagnetic coils (see figure S6), so that the beam is deflected in the x- and y-axes before it interacts with the sample. The deflection makes sure that the scan is captured in a rectangular image pattern. This type

of scanning is called raster scanning, and positions the beam at discrete, but closely spaced, locations on the sample surface [20].

When electrons in the beam reach the sample, they interact with its atoms in the surface or close to it, and two different outgoing signals occur. Each signal has its dedicated detector in the instrument. The signals that are detected for sample analysis include secondary electrons (SEs) – where the beam emitted electrons from the electron gun are called the primary electrons (PEs) – back-scattered electrons (BSEs), and also x-rays [20].

Back-scattered electrons are primary electrons from the beam reflected through elastic scattering after interacting with atoms in the sample [4]. When electrons reach the surface of the sample, some electrons will be absorbed in the sample, while there is another portion that scatter back, completely reversing the initial direction the electrons travelled into the sample, and so they come back out of the sample. These beam electrons being reversed and exited are what is called "backscattered electrons" [20]. More electrons are scattered back the larger the atom is, and so the number of backscattered electrons is proportional to their atomic number. With this information on the sample's composition can be seen on the computer processed image [4]. BSE signals also offer information on topography and crystallography [22][4].

Secondary electrons are electrons that get ejected from the valence or conduction bands of atoms in the sample. SEs occur because of inelastic scattering from the primary electrons from the beam (see figure S7), also they have lower energy than BSEs [23][4]. Concomitantly x-ray signals come about when a primary electron from the beam "knocks out" an inner shell electron. The inner shell has with this become vacant, but its vacancy is restored by an outer shell electron. This process involves a high energy electron moving to a lower energy band in the atom therewith energy must leave the atom as a photon, specifically as x-ray signals energetically characteristic for each element [24].
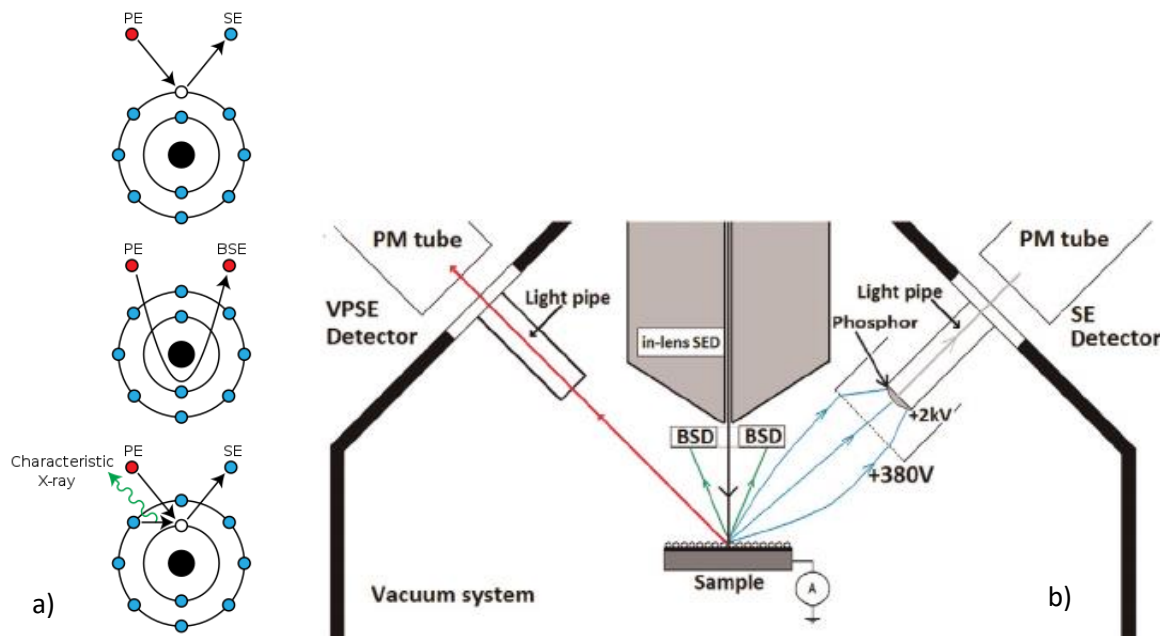
Figure S7. a) Conceptual explanation of PEs interacting with an atomic bond to create SEs and characteristic x-ray signals [25]. b) Schematic drawing of Supra 35VP [26].

When an electron with sufficient energy to scatter inelastically with an electron in the atomic shell is introduced to the atom, it receives an excited state. Excited states don't last long. To return to the ground state – a lower energy state – energy is emitted as an x-ray photon [20], see figure S7.

A.7.2 Detectors and measuring

SEs- and BSEs signals are measured with one or more detectors, see figure S6. It is important that the sample compartment inside the instrument during measurement is carried out under conditions. Atoms and molecules in the atmosphere would otherwise create errorous scattering.

A.7.3 Energy Dispersive X-ray Spectrometry (EDS)

An energy dispersive x-ray spectrometer (EDS) detects photons being dispersed via atomic excitation. For detecting x-rays an EDS detector is attached to the SEM instrument. The x-ray scattering can be used for identification and quantification of the specific elements present in the sample, for the chosen location of the sample surface. X-rays are unique for each element which means it can be used to identify specifically which atoms are contained in the sample. After performing a qualitative analysis has been done, a quantitative can follow. The measured intensity of each element will be proportional to the concentration of it in the given location of sample surface chosen for analysis [20].

A.7.4 Analysing – reading and interpreting the data

Topography is revealed by detecting the number of secondary electrons [27]. More electrons mean higher signal intensity [20]. Detection of back-scattered electrons is also of interest as elements reflect different numbers of electrons, thusly allowing for relative chemical composition by looking at the signal intensities. Heavier elements reflect more electrons which also makes them appear brighter. To find the relative quantity of the elements present in the sample using SEM alone is not feasible. For that analysis EDS is used. The electron beam creates a continuous x-ray spectrum that leads to a spectral background underneath the x-rays interesting for characterisation, and in turn this leads to limited determination of concentrations that can be detected in the sample [28].

A.8 ICP-OES

Inductively coupled plasma optical emission spectroscopy can be used for determination of elemental composition or to quantify the elemental concentration of samples. This is done by detecting electromagnetic radiation (photons) emissions created from atoms reaching an excited state. This is the same principle as in EDS measurements. The wavelength tells which element is present. Unlike magnesium however, lithium cannot be detected by EDS, and so ICP-OES was used for the detection of lithium metal ion uptake. The technique was used to measure the lithium content in the lithium stock solutions, as well as the lithium JA09 and JA10 adsorption experiment sample solutions.

A.8.1 Mechanism

High energy plasma is created from an inert gas, typically argon. This plasma is used to burn the analyte. This creates emission of radiation energy from the analyte. The colour and intensity of the spectral signal picked up from the radiation energy is characteristic and indicative of concentration of the elements contained in the analyte [29].

A.8.2 Preparation

Preparation of calibration requires stock solutions to be prepared. The stock solutions will have known concentration and is used to calculate and determine the analyte concentration. Also, to avoid nanoparticles from compromising the measurement the solutions must be "digested" in acid [29]. The ICP-OES measurement and calculations were performed by faculty member Jorunn H. Vrålstad.

A.9 The Electromagnetic Spectrum (IR)

The electromagnetic spectrum is a spectrum of light of different wavelengths. The spectrum is divided into different respective regions. These have arbitrarily been set. One such region is the region that spans the wavelength spectrum $3.8 \times 10^{-7} m$ to $7.8 \times 10^{-7} m$, which is the region of light that is visible

hence its region name is "visible light" [30]. Visible light passes over to the infrared and ultraviolet regions on its edges.

A.9.1 Infrared spectroscopy (IR)

Infrared spectroscopy (IR) differs from mass spectrometry in that it is non-destructive and in that it involves electromagnetic energy interacting with the molecules rather than an ionising source. IR covers the region of the electromagnetic spectrum from $7.8 \times 10^{-7} m$ to roughly $10^{-4} m$ [30]. In IR measurements electromagnetic energy is beamed at a sample causing molecular vibrations via oscillation of molecular dipoles [31]. The sample will absorb certain wavelengths and pass or transmit other wavelengths [30]. The vibrations are characteristic and depend on the elements, how they are bonded in the structure, and the number of bonds [31]. If the beam consists of a range of different wavelengths it means the absorption spectrum can be determined for the sample. A molecular bond is not fixed, in reality the bond is vibrating at a certain frequency. If the beam hits with a frequency that matches the molecular bond's frequency it translates into amplified vibration of the bond. Like a spring it will compress and stretch further than normal. By relating the vibration – molecular motion – to the frequency, absorbed molecular motions can be determined, and what kinds of bonds they are; that is what functional groups they are [30].

B. Experimental section

B.1 Tables of all syntheses

JA00

Reactants	FW	Molequiv	Amount [g]	Mol
Zr(SO4)2·4H2O	355.396	1	1	0.00281376
trimellitic acid	210.14	1.69123442	1	0.00475873
Solvent (H2O)	72.06	35.0168138	7.1	0.098529

Date 23.09.2021	Theoretical yield	Experimental yield
mol	0.00046896	0.000522161
gram	0.909880809	1.0131
prosent	0.909880809	1.113442541

Table S1. Synthesis of JA00.

JA01

Reactants	FW	Molequiv	Amount [g]	Mol
Zr(SO4)2·4H2O	355.396	1	0.5	0.00140688
trimellitic acid	210.14	4	1.18256818	0.00562753
Solvent (H2O)	72.06	80	8.11038954	0.11255051

Date 24.09.2021	Theoretical yield	Experimental yield
mol	0.00023448	0.000273321
gram	0.454940405	0.5303
prosent	0.909880809	1.165647181

Table S2. Synthesis of JA01.

JA02

Reactants	FW	Molequiv	Amount [g]	Mol
Zr(SO4)2*4H2O	355.4	1	1	0.00281373
H4BTEC	254.15	1.67806414	1.2	0.00472162
Solvent (H2O)	72.06	34.5240078	7	0.09714127
H2SO4	98.079	0.95	-	0.00267304

Date 27.09.2021	Theoretical yield	Experimental yield
mol	0.000468955	0.001339518
gram	0.907019321	*2.5908
prosent	0.907019321	2.856388988

Table S3. Synthesis of JA02. *Product was
still quite wet.

JA03

Reactants	FW	Molequiv	Amount [g]	Mol
Zr(SO4)2*4H2O	355.4	1	1	0.00281373
H4BTEC	254.15	1.67806414	1.2	0.00472162
Solvent (H2O)	72.06	34.5240078	7	0.09714127
H2SO4	98.079	0.95	-	0.00267304

Date 27.09.2021	Theoretical yield	Experimental yield
mol	0.000468955	0.001339518
gram	0.907019321	1.0407
prosent	90.7019321	114.7384599

Table S4. Synthesis of JA03.

JA04

Reactants	FW	Molequiv	Amount [g]	Mol
Zr(SO4)2*4H2O	355.4	1	1	0.00281373
H4BTEC	254.15	0.67	0.479123523	0.0018852
Solvent (H2O)	72.06	27	5.474451322	0.07597074
H2SO4	98.079	0.95	0.143262037	0.00267304

Date 29.09.2021	Theoretical yield	Experimental yield
mol	0.000468955	0.000502345
gram	0.907019321	0.9716
prosent	90.7019321	107.1200996

Table S5. Synthesis of JA04.

JA05

Reactants	FW	Molequiv	Amount [g]	Mol
Zr(SO4)2*4H2O	355.4	1	1	0.00281373
H4BTEC	254.15	0.67	0.479123523	0.0018852
Solvent (H2O)	72.06	27	5.474451322	0.07597074
H2SO4	98.079	0.95	0.143262037	0.00267304

Date 30.09.2021	Theoretical yield	Experimental yield
mol	0.000468955	0.000526646
gram	0.907019321	1.0186
prosent	90.7019321	112.3019076

Table S6. Synthesis of JA05.

JA06

Reactants	FW	Molequiv	Amount [g]	Mol
Zr(SO4)2*4H2O	355.4	1	3	0.00844119
trimellitic acid	210.14	4	7.09532921	0.03376477
Solvent (H2O)	72.06	80	48.6617895	0.67529544

Date 16.11.2021	Theoretical yield	Experimental yield

mol	0.001406866	0.001611786
gram	2.729611705	3.1272
prosent	90.98705684	114.5657455

Table S7. Synthesis of JA06.

JA07

Reactants	FW	Molequiv	Amount [g]	Mol
Zr(SO4)2*4H2O	355.4	1	5	0.01406866
H4BTEC	254.15	0.67	2.395617614	0.009426
Solvent (H2O)	72.06	27	27.37225661	0.37985369
H2SO4	98.079	0.95	-	0.01336522

Date 16.11.2021	Theoretical yield	Experimental yield
mol	0.002344776	0.002259209
gram	4.535096605	4.3696
prosent	90.7019321	96.350759

Table S8. Synthesis of JA07.

JA08

Reactants	FW	Molequiv	Amount [g]	Mol
Zr(SO4)2*4H2O	355.4	1	5	0.01406866
H4BTEC	254.15	0.67	2.395617614	0.009426
Solvent (H2O)	72.06	27	27.37225661	0.37985369
H2SO4	98.079	0.95	0.716310184	0.01336522

Date 17.11.2021	Theoretical yield	Experimental yield
mol	0.002344776	-
gram	4.535096605	-
prosent	90.7019321	-

Table S9. Synthesis of JA08. Sample JA08 was contaminated and could not be used.

JA09

Reactants	FW	Molequiv	Amount [g]	Mol
Zr(SO4)2*4H2O	355.4	1	2	0.00562746
trimellitic acid	210.14	4.5	5.3214969	0.02532358
Solvent (H2O)	72.06	70	28.3860439	0.39392234

Date 19.11.2021	Theoretical yield	Experimental yield
mol	0.00093791	0.001135703
gram	1.819741137	2.2035
prosent	90.98705684	121.0886513

Table S10. Synthesis of JA09. Before measuring sample weight, the sample was first scanned (PXRD) and some sample was lost when grinding and transferring between sample holders.

Washing of JA09 after SEM-EDS measurement: The sample was left to stir in a distilled water solution at 40 °C for 3 hours. Thereafter the sample was washed while being filtrated with Büchner tract. Also, acetone was used in the washing process. Following filtration and washing was drying. The sample was left on the filter paper in the Büchner tract until it was relatively dry, subsequently it was collected on a glass dish, placed in an oven, and left to dry overnight at 80 °C.

JA10

Reactants	FW	Molequiv	Amount [g]	Mol
Zr(SO4)2*4H2O	355.4	1	3	0.00844119
H4BTEC	254.15	0.67	1.437370568	0.0056556
Solvent (H2O)	72.06	27	16.42335397	0.22791221
H2SO4	98.079	0.95	0.42978611	0.00801913

Date 22.11.2021	Theoretical yield	Experimental yield
mol	0.001406866	0.001410093
gram	2.721057963	2.7273
prosent	90.7019321	100.2293974

Table S11. Synthesis of JA10.

B.2 Figures of plots
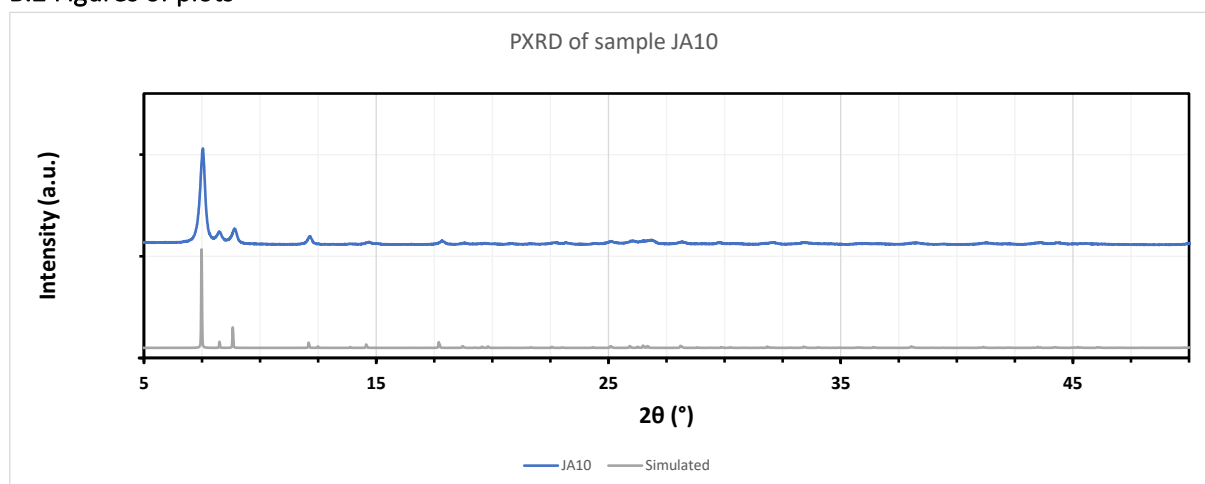
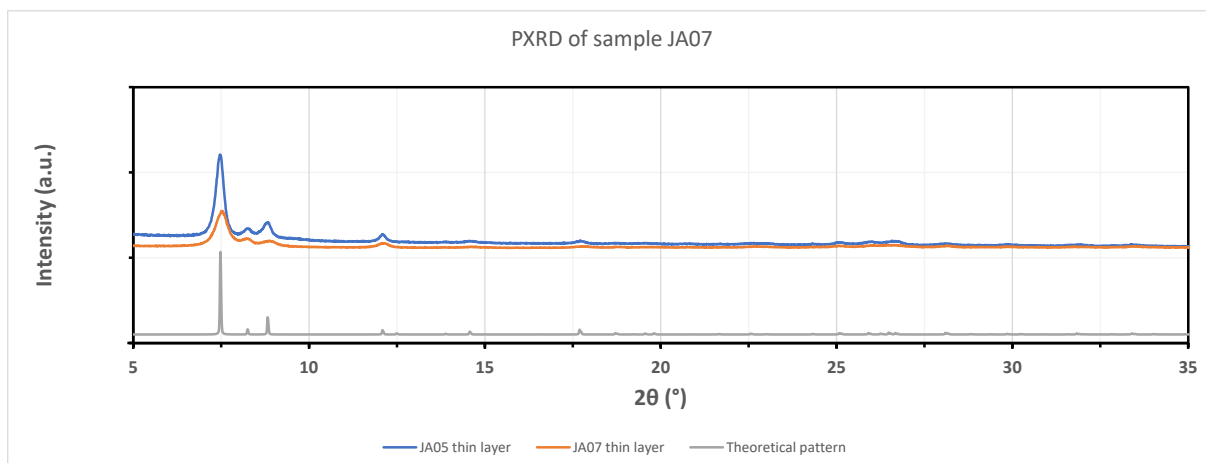Figure S8. PXRD of JA10 – compared to simulated.
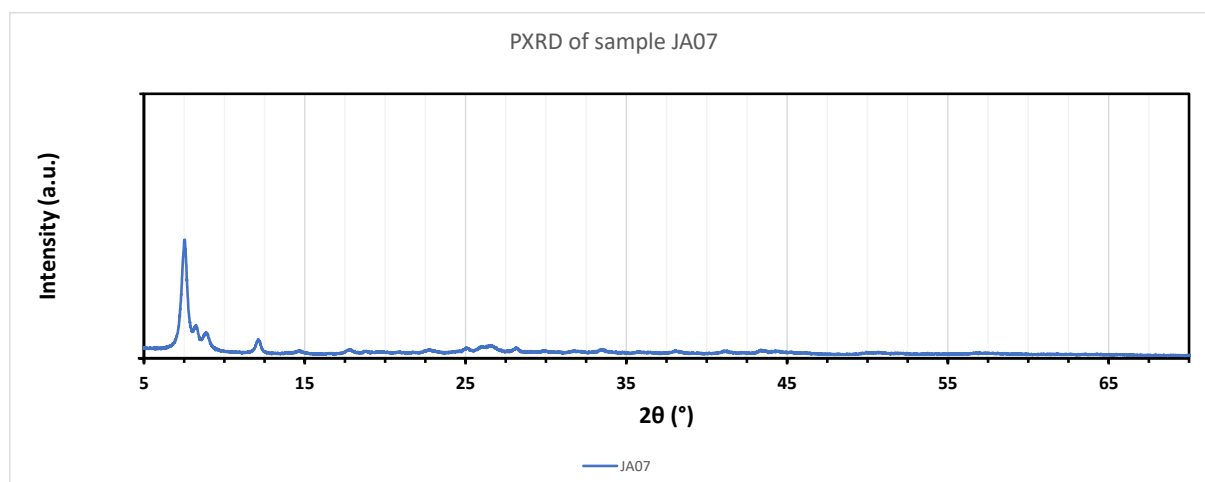
Figure S9. PXRD of JA07.

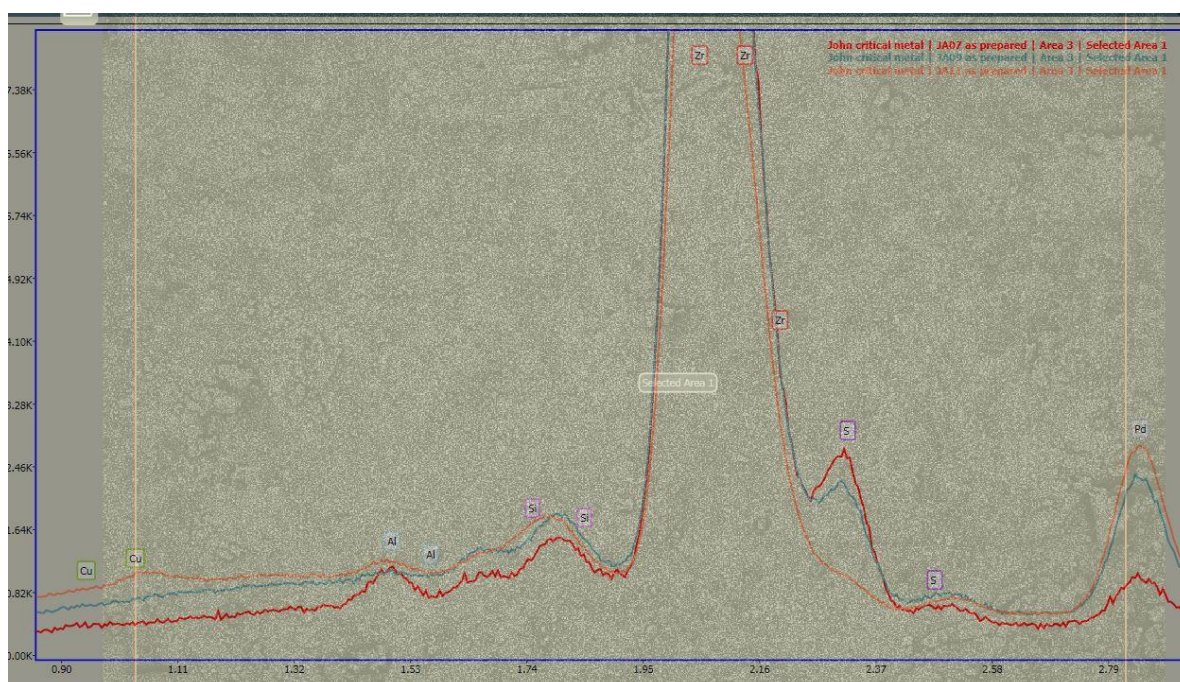Figure S10. PXRD of JA07 – compared to JA05 and simulated.

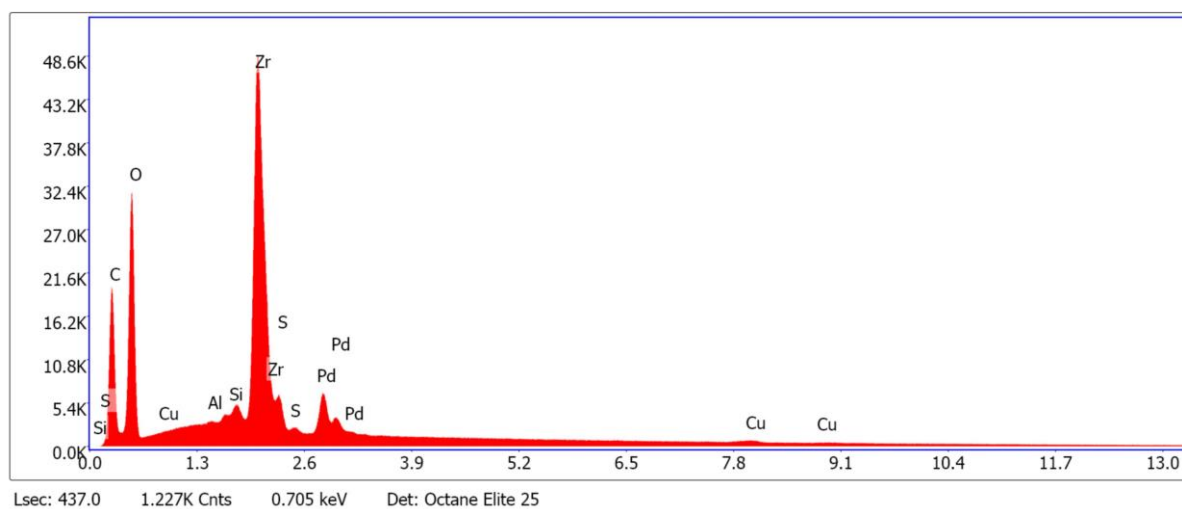Figure S11. Comparison of sample JA09 before and after wasing (zoomed in).
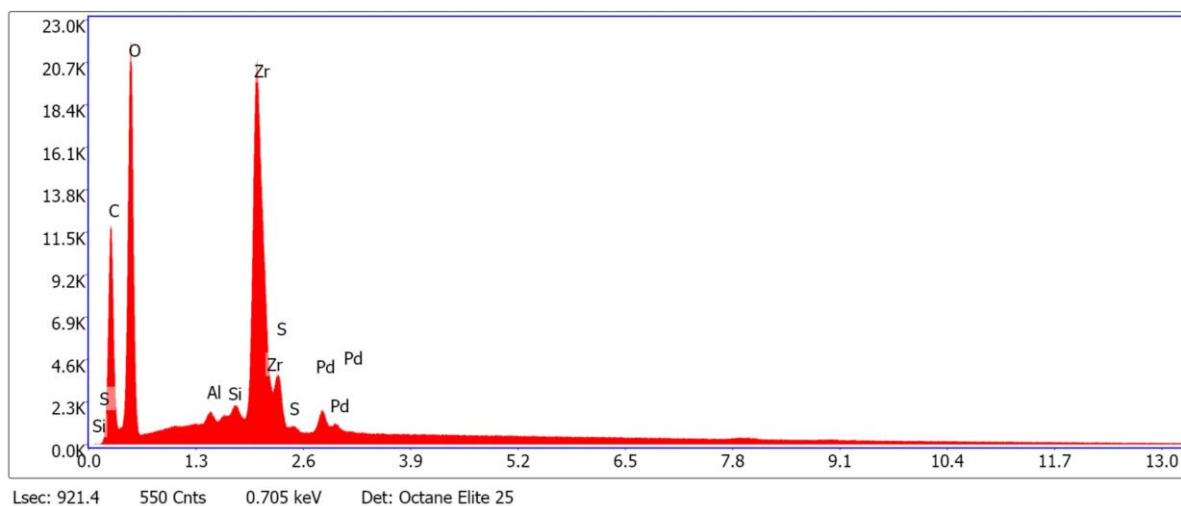

Figure S12. EDS of JA09 as synthesised area 3.

Figure S13. JA10 as synthesised area 1.

Sources of supplement information

[1] University of London. "A little more on Crystal Planes." ucl.ac.uk. http://pd.chem.ucl.ac.uk/pdnn/powintro/planes.htm (Accessed 31.12.2021)

[2] P. M. de Wolff et al., "Nomenclature for crystal families, Bravais-lattice types and arithmetic classes. Report of the International Union of Crystallography Ad-Hoc Committee on the Nomenclature of Symmetry," *Acta Cryst*. (1985). A41, 278-280. https://doi.org/10.1107/S0108767385000587

[3] Bodner Research Web. "Unit cells." purdue.edu. https://chemed.chem.purdue.edu/genchem/topicreview/bp/ch13/unitcell.php (Accessed 31.12.2021)

[4] Illinois Institute of Technology. "Crystal Structures." iit.edu. https://www.iit.edu/sites/default/files/2021-02/crystal_structures.pdf (Accessed 31.12.2021)

[5] H. Wu et al., "Unusual and Highly Tunable Missing-Linker Defects in Zirconium Metal–Organic Framework UiO-66 and Their Important Effects on Gas Adsorption," *J. Am. Chem. Soc*. 2013, 135, 28, 10525–10532. https://doi.org/10.1021/ja404514r

[6] V. V. Butova et al., "UiO-66 type MOFs with mixed-linkers - 1,4-Benzenedicarboxylate and 1,4-naphthalenedicarboxylate: Effect of the modulator and post-synthetic exchange," *Microporous and Mesoporous Materials,* Volume 305, 2020, 110324, ISSN 1387-1811. https://doi.org/10.1016/j.micromeso.2020.110324

[7] S. Yuan et al., "Stable Metal-Organic Frameworks: Design, Synthesis, and Applications," *Adv Mater*. 2018, 30, 1704303. https://doi.org/10.1002/adma.201704303

[8] Andrei A. Bunaciu, Elena gabriela Udriştioiu & Hassan Y. Aboul-Enein, "X-Ray Diffraction: Instrumentation and Applications," *Critical Reviews in Analytical Chemistry,* 2015, 45:4, 289-299. https://doi.org/10.1080/10408347.2014.949616

[9] W. Ockenga. Phase Contrast. "Making Unstained Phase Objects Visible." leica-microsystems.com. https://www.leica-microsystems.com/science-lab/phase-contrast/ (Accessed 31.12.2021)

[10] Wikipedia. "File:Bragg diffraction 2.svg." wikipedia.org. https://en.wikipedia.org/wiki/File:Bragg_diffraction_2.svg (Accessed 31.12.2021)

[11] PerkinElmer. "A Beginner's Guide to Thermogravimetric Analysis." perkinelmer.com. https://resources.perkinelmer.com/lab-solutions/resources/docs/FAQ_Beginners-Guide-to-Thermogravimetric-Analysis_009380C_01.pdf (Accessed 31.12.2021)

[12] D. Banerjee. "Experimental Techniques in Thermal Analysis Thermogravimetry (TG) & Differential Scanning Calorimetry (DSC)." iitk.ac.in. https://www.iitk.ac.in/che/pdf/resources/TGA-DSC-reading-material.pdf (Accessed 31.21.2021)

[13] Doran Pauline M. (2013). *Bioprocess Engineering Principles, Second edition*. 225 Wyman Street, Waltham, MA 02451, USA: Elsevier Ltd.

[14] G. Limousin, J.-P. Gaudet, L. Charlet, S. Szenknect, V. Barthès, M. Krimissa, "Sorption isotherms: A review on physical bases, modeling and measurement," *Applied Geochemistry*, Volume 22, Issue 2, 2007, Pages 249-275, ISSN 0883-2927. https://doi.org/10.1016/j.apgeochem.2006.09.010

[15] K.Y. Foo, B.H. Hameed, "Insights into the modeling of adsorption isotherm systems," *Chemical Engineering Journal*, Volume 156, Issue 1, 2010, Pages 2-10, ISSN 1385-8947. https://doi.org/10.1016/j.cej.2009.09.013

[16] Thommes M. et al., (2015). "Physisorption of gases, with special reference to the evaluation of surface area and pore size distribution (IUPAC Technical Report)." *Pure and Applied Chemistry.* DOI 10.1515/pac-2014-1117

[17] Rouquerol, Jean & Llewellyn, Philip & Rouquerol, F.. (2007). "Is the BET Equation Applicable to Microporous Adsorbents?" *Studies in Surface Science and Catalysis*. 160. 49-56. DOI:10.1016/S0167-2991(07)80008-5

[18] Diego A. Gómez-Gualdrón, Peyman Z. Moghadam, Joseph T. Hupp, Omar K. Farha, and Randall Q. Snurr, "Application of Consistency Criteria To Calculate BET Areas of Micro- And Mesoporous Metal–Organic Frameworks," *J. Am. Chem. Soc*. 2016, 138, 1, 215–224. https://doi.org/10.1021/jacs.5b10266

[19] K. Peikert. "Gas Sorption Characterization of Metal Organic Frameworks Webinar." micromeritics.com. https://www.micromeritics.com/gas-sorption-characterization-of-metal-organic-frameworks-webinar/ (Accessed 31.12.2021)

[20] J. I. Goldstein, D. E. Newbury, J. R. Michael, M. W. Ritchie, J. H. J. Scott, D. C. Joy, "Electron Beam - Specimen Interactions: Interaction Volume," in Scanning Electron Microscopy and X-Ray Microanalysis, 4. edition. Land: New York, NY 10013, U.S.A: Springer Nature, 2018, chapter 1, p. 1 – 14. [Online]. https://link.springer.com/content/pdf/10.1007/978-1-4939-6676-9.pdf

[21] Wikipedia. "File:Schema MEB (en).svg." wikipedia.org. https://en.wikipedia.org/wiki/File:Schema_MEB_(en).svg (Accessed 31.12.2021)

[22] J. I. Goldstein, D. E. Newbury, J. R. Michael, M. W. Ritchie, J. H. J. Scott, D. C. Joy, "Backscattered Electrons," in Scanning Electron Microscopy and X-Ray Microanalysis, 4. edition. Land: New York, NY 10013, U.S.A: Springer Nature, 2018, chapter 1, p. 15 – 28. [Online]. https://link.springer.com/content/pdf/10.1007/978-1-4939-6676-9.pdf

[23] J. I. Goldstein, D. E. Newbury, J. R. Michael, M. W. Ritchie, J. H. J. Scott, D. C. Joy, "Secondary Electrons," in Scanning Electron Microscopy and X-Ray Microanalysis, 4. edition. Land: New York, NY 10013, U.S.A: Springer Nature, 2018, chapter 1, p. 29 – 37. [Online]. https://link.springer.com/content/pdf/10.1007/978-1-4939-6676-9.pdf

[24] J. I. Goldstein, D. E. Newbury, J. R. Michael, M. W. Ritchie, J. H. J. Scott, D. C. Joy, «X-Rays,» in Scanning Electron Microscopy and X-Ray Microanalysis, 4. edition. Land: New York, NY 10013, U.S.A: Springer Nature, 2018, chapter 1, p. 39 – 63. [Online]. https://link.springer.com/content/pdf/10.1007/978-1-4939-6676-9.pdf

[25] Wikipedia. "File:Electron emission mechanisms.svg" wikipedia.org. https://en.wikipedia.org/wiki/File:Electron_emission_mechanisms.svg (Accessed 31.12.2021)

[26] Engelsen, Daniel & Harris, Paul & Ireland, T. & Fern, George & Silver, Jack. (2015). "Contrast and decay of cathodoluminescence from phosphor particles in a scanning electron microscope." *Ultramicroscopy*. DOI:10.1016/j.ultramic.2015.05.009

[27] A. Nanakoudis. "SEM: Types of Electrons and the Information They Provide." ThermoFisher.com. https://www.thermofisher.com/blog/microscopy/sem-signal-types-electrons-and-the-information-they-provide/ (Accessed 31.12.2021)

[28] J. I. Goldstein, D. E. Newbury, J. R. Michael, M. W. Ritchie, J. H. J. Scott, D. C. Joy, "X-Rays," in Scanning Electron Microscopy and X-Ray Microanalysis, 4. edition. Land: New York, NY 10013, U.S.A: Springer Nature, 2018, chapter 1, p. 39 – 63. [Online]. https://link.springer.com/content/pdf/10.1007/978-1-4939-6676-9.pdf

[29] P. M. V. Raja and A. R. Barron. "ICP-AES Analysis of Nanoparticles." Libretexts.org. https://chem.libretexts.org/Bookshelves/Analytical_Chemistry/Physical_Methods_in_Chemistry_and_Nano_Science_(Barron)/01:_Elemental_Analysis/1.05:_ICP-AES_Analysis_of_Nanoparticles (Accessed 31.12.2021)

[30] John McMurry, Ralph J. Fessenden, Joan S Fessenden, and Patty Feist, "Structure Determination: Mass Spectrometry, Infrared Spectrometry, and Ultraviolet Spectroscopy," in KJE200 Organisk Kjemi, Custom Edition. Stavanger 2018, United Kingdom: Cengage Learning EMEA, 2018, chapter 10., page 403 – 410.

[31] P. M. V. Raja and A. R. Barron. "IR Spectroscopy." Libretexts.org. https://chem.libretexts.org/Bookshelves/Analytical_Chemistry/Physical_Methods_in_Chemistry_and_Nano_Science_(Barron)/04:_Chemical_Speciation/4.02:_IR_Spectroscopy (Accessed 31.12.2021)